Soft Information-Based Localization for 5G Networks and Beyond

Flavio Morselli, Sara Modarres Razavi, Moe Z. Win, *Fellow, IEEE*, and Andrea Conti, *Fellow, IEEE*

***Abstract*— Accurate location information is crucial for a variety of new verticals and use cases enabled by 5th generation (5G) wireless networks. While existing localization techniques for cellular networks are continuously evolving in the standardization process, the stringent key performance indicator requirements defined by the 3rd Generation Partnership Project (3GPP) have not been met yet. This paper first provides an in-depth review of the standardized reference signals and time/angle-based measurements that can be used for localization of user equipments in current 5G networks. Then, the paper details the development of a soft information (SI)-based approach that significantly improves localization accuracy for 5G and beyond 5G networks. Results are obtained in full conformity with 3GPP standards in two standardized scenarios, namely urban microcell and indoor open office, using time/angle-based measurements. Results show that the proposed SI-based localization methods significantly outperform existing techniques, especially when harsh propagation conditions and higher (millimeter Waves) frequencies are considered, paving the way to new services and performance enhancements in 5G and beyond wireless networks.**

***Index Terms*— Localization, 5G, 3GPP, machine learning, wireless networks.**

I. Introduction

LOCATION AWARENESS [1], [2], [3], [4], [5], [6], [7], [8] is critical for many verticals and use cases (UCs) enabled by 5th generation (5G) networks and beyond 5G networks, including autonomy [9], [10], [11], [12], [13], crowd-sensing [14], [15], [16], [17], [18], smart environments [19], [20], [21], [22], [23], and the Internet-of-Things [24], [25], [26], [27], [28]. Moreover, the location information of user equipments (UEs) is a valuable asset that allows service providers to perform smart network management based on the users' position [29], [30], [31], [32], [33], [34]. The 3rd Generation Partnership Project (3GPP) standardization body has defined UCs in which networks rely on location awareness for different verticals; each UC defines different requirements on key performance indicators (KPIs) including horizontal and vertical localization accuracy, service availability, and maximum latency [35], [36]. Such requirements are grouped, by the 3GPP, in seven positioning service levels as reported in Tab. I. However, providing localization functionalities that satisfy the KPI requirements is challenging, especially in harsh wireless environments.

TABLE I
KPI Requirements for the Different Positioning Service Levels: (A) and (R) Denote Absolute and Relative Localization Accuracy, Respectively

Service Level	Horizontal Accuracy	Vertical Accuracy	Availability	Latency
1	10 m (A)	3 m (A)	99%	1 s
2	3 m (A)	3 m (A)	99%	1 s
3	1 m (A)	2 m (A)	99%	1 s
4	1 m (A)	2 m (A)	99.9%	15 ms
5	0.3 m (A)	2 m (A)	99%	1 s
6	0.3 m (A)	2 m (A)	99.9%	10 ms
7	0.2 m (R)	0.2 m (R)	99%	1 s

Current long-term evolution and 5G networks rely on proximity information, fingerprints, or single-value estimates (SVEs) such as time and power estimates for localization [37], [38], [39]. For example in enhanced-cell ID methods, a coarse estimate of the UE position is determined based on the ID of the base station serving the UE, and on position-related time-based or power-based metrics extracted from the received signals. In the case of downlink time-difference-of-arrival (DL-TDOA), the differences between the arrival times (received at the UE) of a reference signal (RS) (transmitted from different base stations) are used for inferring the UE's position. In Release 16 (Rel-16) and Rel-17, the 3GPP standardization activities related to 5G Radio Access Network positioning have been focused on leveraging new types of time measurements and of angle information enabled by features of 5G networks such as large antenna arrays in SVE-based localization methods [38], [39]. Currently, a study item in 3GPP is evaluating the potential benefits of artificial intelligence and machine learning for 5G air interface

Manuscript received 25 February 2022; revised 5 August 2022 and 16 January 2023; accepted 18 April 2023. Date of publication 16 May 2023; date of current version 12 December 2023. The fundamental research described in this paper was supported in part by the European Union's Horizon 2020 Research and Innovation Programme under Grant 871249, in part by the Office of Naval Research under Grant N62909-22-1-2009, in part by the National Science Foundation under Grant CNS-2148251, and in part by the Federal Agency and Industry Partners in the RINGS Program. The associate editor coordinating the review of this article and approving it for publication was K. Zhang. *(Corresponding author: Andrea Conti.)*

Flavio Morselli and Andrea Conti are with the Department of Engineering and CNIT, University of Ferrara, 44122 Ferrara, Italy (e-mail: flavio.morselli@unife.it; a.conti@ieee.org).

Sara Modarres Razavi is with Ericsson, 164 80 Stockholm, Sweden (e-mail: sara.modarres.razavi@ericsson.com).

Moe Z. Win is with the Laboratory for Information and Decision Systems (LIDS), Massachusetts Institute of Technology, Cambridge, MA 02139 USA (e-mail: moewin@mit.edu).

Color versions of one or more figures in this article are available at https://doi.org/10.1109/TWC.2023.3275122.

Digital Object Identifier 10.1109/TWC.2023.3275122

within the scope of the upcoming Rel-18 [40], including for enhancing localization accuracy.

Existing SVE-based localization techniques have not yet managed to fulfill the stringent KPI requirements defined by 3GPP, especially in harsh wireless propagation environments due to multipath propagation and non-line-of-sight (NLOS) conditions [41], [42]. Time-based methods relying on dedicated RSs such as DL-TDOA based on the positioning reference signal (PRS) and uplink time-difference-of-arrival (UL-TDOA) based on the sounding reference signal (SRS) can provide higher localization accuracy than proximity-based counterparts. The design of localization techniques has been mainly focused on DL-TDOA measurements obtained from 5G networks operating in frequency range 1 (FR1), i.e., employing carrier frequencies below 7.125 GHz [43]. However, other types of time-based measurements such as UL-TDOA based on SRS and multi-cell round trip time (MRTT) measurements based on both PRS and SRS can be exploited to perform localization [44]. Considering wireless networks operating in frequency range 2 (FR2), i.e., employing millimiter Waves with carrier frequency in the range from 24.25 GHz to 52.6 GHz [43], angle-based measurements enabled by the use of multiple antennas such as angle-of-departure (AOD) measurements can also be exploited individually or together with time-based measurements [44], [45].

Recently, a new localization approach based on soft information (SI) [46], [47], [48], [49], [50] has been proposed as an alternative to SVE-based localization (see Fig. 1 for a pictorial depiction of SI-based localization). SI-based localization relies on probabilistic models learned from the environment via machine learning techniques to characterize the relationship between the measurements and UE locations. In [48], the advantages of SI-based localization for 5G networks and beyond have been demonstrated and the performance gains provided by the SI-based approach have been quantified in specific scenarios and network settings considering time measurements (i.e., DL-TDOA measurements). Furthermore, the benefits of fusing radio access technology (RAT)-dependent measurements (i.e., measurements obtained using 5G technology) and RAT-independent measurements (i.e., measurements obtained using non-3GPP technologies such as Wi-Fi) through the SI framework were investigated in [49].

SI-based localization represents a good candidate for providing accurate localization in 5G networks and beyond, owing to its improved accuracy compared to SVE-based approaches and to the possibility of fusing heterogeneous measurements in a seamless way. The fundamental questions related to SI-based localization in 5G and beyond networks are:

- how to design SI-based techniques capable of exploiting all types of RAT-dependent measurements provided by 5G networks at different frequency ranges; and
- which advantages can SI-based localization provide by leveraging new 5G measurements and by fusing different RAT-dependent measurements?

The answers to these questions will enhance the localization capabilities of 5G and beyond networks, enabling new verticals relying on accurate location information of UEs. The goal of this work is to develop SI-based localization methods and demonstrate that SI-based approach is able to leverage all types of 5G measurements and achieves tangible improvements in localization accuracy compared to existing approaches. We advocate the use of SI-based approach for localization in 5G and beyond networks, leveraging generative models learned from the wireless environment via machine learning techniques. Such approach can easily be integrated into the already standardized 5G localization procedures and architecture.

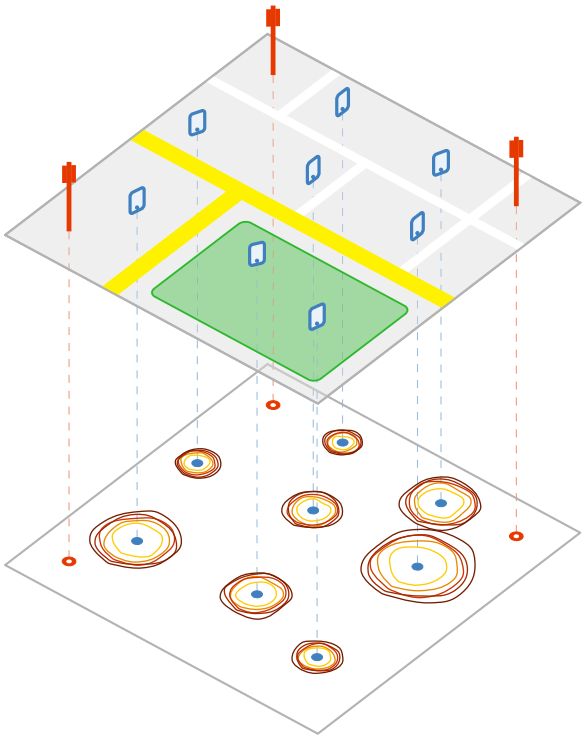

Fig. 1. Pictorial view of location awareness provided by SI-based localization: blue dots represent the UEs, red annuluses represent the next generation NodeBs (gNBs), and the yellow-red contour lines represent the SI associated with the UE positions. Lighter colors are associated with higher values of SI, i.e., lower uncertainty regarding the UE positions.

This paper develops SI-based localization methods that can be easily integrated into the network architecture for 5G and beyond. The localization performance is assessed in two standardized scenarios, namely indoor open office (IOO) and urban microcell (UMi), via a simulator that we developed in full conformity with 3GPP technical reports [51]. The key contributions of this paper can be summarized as follows:

- review of PRS, SRS, and time/angle-based measurements according to 3GPP specifications, as well as a discussion of existing localization algorithms;
- design of SI-based localization methods that can fuse heterogeneous measurements, including DL-TDOA, UL-TDOA, MRTT, and AOD measurements;
- quantification of the performance gain provided by SI-based localization methods compared to existing techniques in 3GPP IOO and UMi scenarios; and
- evaluation of the impact of generative model complexity and training set size on the SI-based localization accuracy.

The remainder of the paper is organized as follows: Sec. II gives a review of the 5G RSs involved in the localization

process; Sec. III describes the localization process based on RAT-dependent measurements; Sec. IV introduces the notion of SI-based localization for 5G and beyond networks; Sec. V presents the performance of 5G localization based on SI and compares it with existing 5G localization based on SVEs; and Sec. VI gives our conclusion.

Notation: Random variables (RVs) are displayed in sans serif, upright fonts; their realizations in serif, italic fonts. Vectors and matrices are denoted by bold lowercase and uppercase letters, respectively. For example, a RV and its realization are denoted by x and x; a random vector and its realization are denoted by $\mathbf{x}$ and $\boldsymbol{x}$; a random matrix and its realization are denoted by $\mathbf{X}$ and $\boldsymbol{X}$, respectively. Random sets and their realizations are denoted by up-right sans serif and calligraphic font, respectively. For example, a random set and its realization are denoted by X and $\mathcal{X}$, respectively. The function $f_{\mathbf{x}}(\boldsymbol{x})$ and, for brevity when possible, $f(\boldsymbol{x})$ denote the probability density function (PDF) of a vector of continuous RVs $\mathbf{x}$; $f_{\mathbf{x}|\mathbf{y}}(\boldsymbol{x}|\boldsymbol{y})$ and, for brevity when possible, $f(\boldsymbol{x}|\boldsymbol{y})$ denote the PDF of $\mathbf{x}$ conditional on $\mathbf{y} = \boldsymbol{y}$; $\varphi(\boldsymbol{x}; \boldsymbol{\mu}, \boldsymbol{\Sigma})$ denotes the PDF of a Gaussian RV $\mathbf{x}$ with mean $\boldsymbol{\mu}$ and covariance matrix $\boldsymbol{\Sigma}$; operator $\mathbb{E}\{\cdot\}$ denotes the expectation of the argument. For a matrix $\boldsymbol{A}$ and a vector $\boldsymbol{a}$, the transpose is respectively denoted by $\boldsymbol{A}^{\mathrm{T}}$ and $\boldsymbol{a}^{\mathrm{T}}$. Operators $(\cdot)^*$ and $||\cdot||_2$ denote the complex conjugate operator and the 2-norm, respectively. The imaginary unit is denoted by $\jmath$.

II. 5G Measurements for Localization

5G networks support six different RAT-dependent measurements and their combinations for providing localization functionality [52]. This work focuses on time-based methods (i.e., DL-TDOA, UL-TDOA, and MRTT measurements) and angle-based methods (i.e., AOD measurement). In particular, the PRS and SRS involved in the localization process are described below.[1] Hereafter, 5G RSs and low complexity algorithms for obtaining measurements according to the 5G standardized architecture are presented.[2]

A. Positioning Reference Signal

The PRS was introduced in 3GPP Rel-9 [53] and it has been updated for 5G wireless networks by expanding its flexibility in terms of frequency and time slot allocation. Similar to long-term evolution, PRS for 5G uses slots where no data are transmitted. The sequence used to generate the PRS is a 31-bit long Gold sequence $c[m]$, where the seed $c_{\mathrm{init}}^{\mathrm{PRS}}$ depends on the physical cell identity (PCI) and on the values assumed in the set $\{0, 1, \ldots, 4095\}$ [54].

The binary sequence $c[m]$ is then modulated via quadrature phase-shift keying-modulation as

$$s[m] = \frac{1}{\sqrt{2}}\Big(1 - 2c[m]\Big) + \jmath\frac{1}{\sqrt{2}}\Big(1 - 2c[m+1]\Big). \quad (1)$$

[1]The notation used throughout Sec. II is in conformity with 3GPP technical specifications and reports.

[2]Algorithms for determining time and angle estimates based on 5G RSs are not standardized by 3GPP and their implementation is left to the network vendor.

The symbols $s[m]$ are mapped to the (l, k) resource element (RE), i.e., the k-th subcarrier (SC) of the l-th symbol, over a specific time-frequency pattern as described in detail in [54]. In the frequency domain, the PRS is arranged in a comb structure, i.e., only one SC out of $K_{\mathrm{comb}}^{\mathrm{PRS}}$ SCs is effectively used for transmitting the symbols $s[m]$, while the other $(K_{\mathrm{comb}}^{\mathrm{PRS}} - 1)$ SCs are padded with zeros. This particular frequency structure allows for interference suppression in case of multiple PRS transmissions from different gNBs. The comb size $K_{\mathrm{comb}}^{\mathrm{PRS}}$ is configurable within the values $\{2, 4, 6, 12\}$. In the time domain, the PRS occupies $L_{\mathrm{PRS}} \in \{2, 4, 6, 12\}$ consecutive symbols within a slot and the starting PRS symbol within a slot denoted by $l_{\mathrm{start}}^{\mathrm{PRS}}$, can be configured.

Given a specific numerology $\mu \in \{0, 1, 2, 3, 4\}$, i.e., a specific SC spacing determined by $\Delta_{\mathrm{f}} = 2^{\mu} \times 15\,\mathrm{KHz}$, the (l, k) RE for a PRS transmission can be written as

$$a_{k,l}^{(\mu)} = \begin{cases} \beta_{\mathrm{PRS}}\, s[m] & \text{if } m \text{ is mapped to } k \\ 0 & \text{otherwise} \end{cases} \quad (2)$$

for $k = 0, 1, \ldots, N_{\mathrm{FFT}}^{\mathrm{PRS}} - 1$ and $l = l_{\mathrm{start}}^{\mathrm{PRS}}, l_{\mathrm{start}}^{\mathrm{PRS}} + 1, \ldots, l_{\mathrm{start}}^{\mathrm{PRS}} + L_{\mathrm{PRS}} - 1$, where β_{PRS} is a scale coefficient. The detailed procedure used to map the modulated symbols to the SCs can be found in [54]. The quantity $N_{\mathrm{FFT}}^{\mathrm{PRS}}$ represents the number of SCs allocated for PRS transmission and is defined as

$$N_{\mathrm{FFT}}^{\mathrm{PRS}} = N_{\mathrm{SC}}^{\mathrm{RB}} N_{\mathrm{RB}}^{\mathrm{PRS}} \quad (3)$$

where $N_{\mathrm{SC}}^{\mathrm{RB}} = 12$ is the number of SC per resource block (RB) and $N_{\mathrm{RB}}^{\mathrm{PRS}}$ is the number of RBs allocated for the PRS. Given $N_{\mathrm{FFT}}^{\mathrm{PRS}}$, the digital orthogonal frequency division multiplexing modulated signal for the l-th symbol is obtained via inverse fast Fourier transform as

$$s_l[n] = \frac{1}{\sqrt{N_{\mathrm{FFT}}^{\mathrm{PRS}}}} \sum_{k=0}^{N_{\mathrm{FFT}}^{\mathrm{PRS}}-1} a_{k,l} \exp\left\{2\pi \frac{nk}{N_{\mathrm{FFT}}^{\mathrm{PRS}}}\right\} \quad (4)$$

where the superscript (μ) in (2) is omitted in (4) for notation simplicity. The digital signal $s_l[n]$ is then converted to a continuous-time signal and modulated to radio frequency.

In order to facilitate the PRS reception procedure, the time slots allocated for PRS transmission are organized into three different interrelated logical entities: (i) positioning frequency layers; (ii) PRS resource sets; and (iii) PRS resources. Each entity determines a subset of parameters defining the PRS and the three entities follows a hierarchic relationship as follows: different PRS resources are grouped in a PRS resource set, and PRS resource sets are grouped in a positioning frequency layer. In particular, the PRS time signal is transmitted when the quantity $z(n_{\mathrm{f}}, n_{\mathrm{s,f}}^{\mu})$, which depends on the system frame number n_{f} and slot number $n_{\mathrm{s,f}}^{\mu}$, fulfills the condition

$$\Big(z(n_{\mathrm{f}}, n_{\mathrm{s,f}}^{\mu}) \mod 2^{\mu} T_{\mathrm{per}}^{\mathrm{PRS}}\Big) \in \Big\{n T_{\mathrm{gap}}^{\mathrm{PRS}}\Big\}_{n=0}^{T_{\mathrm{rep}}^{\mathrm{PRS}}-1} \quad (5)$$

where $T_{\mathrm{per}}^{\mathrm{PRS}} \in \{4, 5, 8, 10, 16, 20, 32, 40, 64, 80, 160, 320, 640, 1280, 2560, 5120, 10240\}$ is the PRS transmission periodicity, $T_{\mathrm{gap}}^{\mathrm{PRS}} \in \{1, 2, 4, 8, 16, 32\}$ is the time gap in slots between two instances of PRS resource belonging to the same set, $T_{\mathrm{rep}}^{\mathrm{PRS}} \in \{1, 2, 4, 6, 8, 16, 32\}$ is the number of repeated PRS

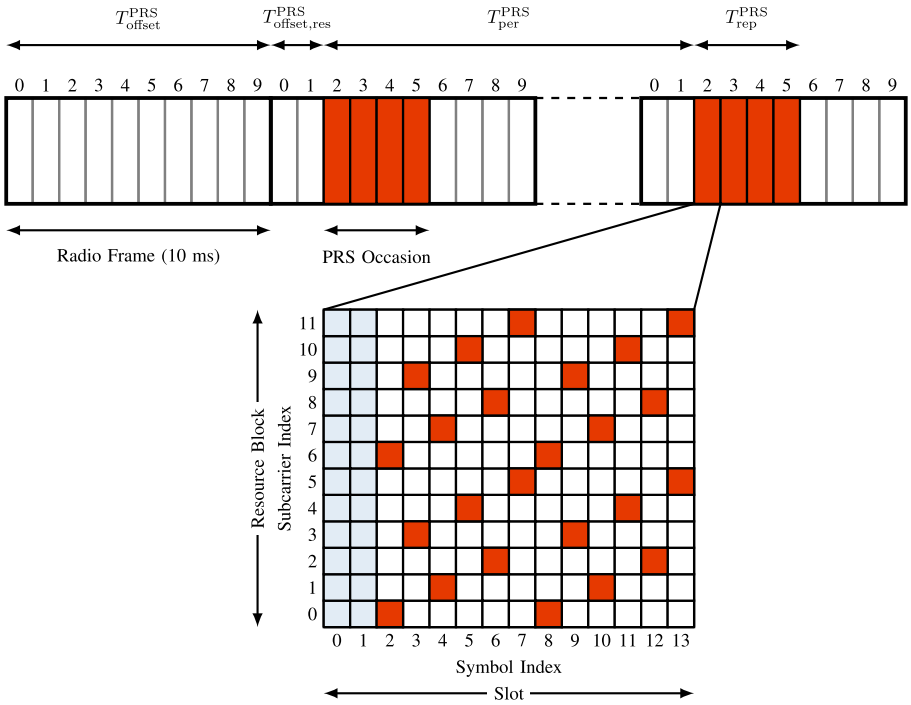

Fig. 2. Example of PRS occasions considering the numerology $\mu = 0$, i.e., where one slot occupies an entire subframe [54]. In the example, $T^{\mathrm{PRS}}_{\mathrm{offset}} = 10$, $T^{\mathrm{PRS}}_{\mathrm{offset,res}} = 2$, $T^{\mathrm{PRS}}_{\mathrm{gap}} = 1$, and $T^{\mathrm{PRS}}_{\mathrm{rep}} = 4$. For the time-frequency allocation of the PRS in one RB, the parameters in the example are: $K^{\mathrm{PRS}}_{\mathrm{comb}} = 6$, $l^{\mathrm{PRS}}_{\mathrm{start}} = 2$, and $L_{\mathrm{PRS}} = 12$.

slots in a single instance of PRS resource set. The quantity $z(n_{\mathrm{f}}, n^{\mu}_{\mathrm{s,f}})$ is defined as

$$z(n_{\mathrm{f}}, n^{\mu}_{\mathrm{s,f}}) = N^{\mathrm{frame},\mu}_{\mathrm{slot}} n_{\mathrm{f}} + n^{\mu}_{\mathrm{s,f}} - T^{\mathrm{PRS}}_{\mathrm{offset}} - T^{\mathrm{PRS}}_{\mathrm{offset,res}} \quad (6)$$

where $N^{\mathrm{frame},\mu}_{\mathrm{slot}}$ is the number of slots within a radio frame, $T^{\mathrm{PRS}}_{\mathrm{offset}} \in \{0, 1, \ldots, T^{\mathrm{PRS}}_{\mathrm{per}} - 1\}$ is the slot offset relative to the system frame number zero (i.e., $n_{\mathrm{f}} = 0$), and $T^{\mathrm{PRS}}_{\mathrm{offset,res}}$ is the slot offset of the PRS resource with respect to the offset $T^{\mathrm{PRS}}_{\mathrm{offset}}$.[3] From [55], a PRS resource is defined by: a unique identifier for resource within the PRS resource set; the slot offset of the PRS resource with respect to the slot offset of the PRS resource set; the RB offset with respect to the index of SC zero in the allocated resource grid; the seed used to generate the PRS sequence; the index $l^{\mathrm{PRS}}_{\mathrm{start}}$ corresponding to the first PRS symbols in the slot; a list of other resources in the same PRS resource set; and an indicator of other RSs experiencing or not similar channel conditions as the PRS. Each instantiation of a PRS resource is referred to as a PRS occasion. A PRS resource set is defined by a resource set ID, the time allocation parameters $T^{\mathrm{PRS}}_{\mathrm{per}}$, $T^{\mathrm{PRS}}_{\mathrm{rep}}$, $T^{\mathrm{PRS}}_{\mathrm{gap}}$ (configured only if $T^{\mathrm{PRS}}_{\mathrm{rep}} \neq 1$), a bit map representing a muting pattern for the transmission, $T^{\mathrm{PRS}}_{\mathrm{offset}}$, $T^{\mathrm{PRS}}_{\mathrm{offset,res}}$, the comb size $K^{\mathrm{PRS}}_{\mathrm{comb}}$, the number of symbols L_{PRS}, and the bandwidth allocated for the PRS defined in terms of RB, $N^{\mathrm{PRS}}_{\mathrm{RB}}$, starting from a minimum of 24 to a maximum of 272, with a granularity of 4. The positioning frequency layer defines the SC spacing of all the PRS resource sets belonging to the layer, the cyclic prefix used for the transmission, and the absolute frequency point for the resource grid allocated for the PRS transmission. Fig. 2 depicts multiple 5G radio frames with two PRS occasions. The time-frequency grid of the PRS signal is also depicted for a particular set of parameters.

[3]Additional conditions and constraints on the transmission of the PRS resource set and resource are present if muting patterns are provided [55].

B. Sounding Reference Signal

The SRS is an uplink RS used for both communication and localization purposes. For communication purposes, the SRS is used to perform uplink channel sounding, which includes channel estimation for precoding and timing control. For localization purposes, the SRS is used to obtain UL-TDOA and, in conjunction with the PRS, MRTT measurements. SRS for communication and SRS for localization share similar features with different configurations.

The SRS and PRS share a similar time-frequency structure, with SRS exhibiting a comb pattern in the frequency domain, governed by the comb size parameter $K^{\mathrm{SRS}}_{\mathrm{comb}}$. SRS is transmitted in L_{SRS} consecutive symbols within an allocated time slot, starting from the symbol indexed by $l^{\mathrm{SRS}}_{\mathrm{start}}$. The values allowed for the parameters are $K^{\mathrm{SRS}}_{\mathrm{comb}} \in \{2, 4, 8\}$ and $L_{\mathrm{SRS}} \in \{1, 2, 4, 8, 12\}$. In contrast to the PRS, the SRS uses a complex-valued Zadoff–Cho sequence $c_{\mathrm{zc}}[m]$ as base signal in order to ensure a low level of peak-to-average-power ratio [54]. The specific sequence employed depends on the values of $K^{\mathrm{SRS}}_{\mathrm{comb}}$ and L_{SRS}. Similarly to (2), the RE for a SRS transmission can be written as

$$a_{k,l} = \begin{cases} \beta_{\mathrm{SRS}}\, c_{\mathrm{zc}}[m] & \text{if } m \text{ is mapped to } k \\ 0 & \text{otherwise} \end{cases} \quad (7)$$

for $l = l_{\text{start}}^{\text{SRS}}, l_{\text{start}}^{\text{SRS}}+1, \ldots, l_{\text{start}}^{\text{SRS}}+L_{\text{SRS}}-1$ and $k = 0, 1, \ldots, N_{\text{FFT}}^{\text{SRS}}$, where β_{SRS} is a scale factor. The detailed procedure used to determine $c_{\text{zc}}[m]$, as well as how the sequence is mapped to the SCs, can be found in [54]. Given $a_{k,l}$, the orthogonal frequency division multiplexing signal is obtained as in (4), with $N_{\text{FFT}}^{\text{SRS}} = N_{\text{SC}}^{\text{RB}} N_{\text{RB}}^{\text{SRS}}$, where $N_{\text{RB}}^{\text{SRS}}$ is the number of RBs for SRS transmission.

Similar to PRS, SRS transmissions for localization are organized in time as SRS resource, i.e., collections of multiple SRS slots, and multiple SRS resources are collected in a SRS resource set. The transmission of an SRS resource can be configured to be periodic, but differently from the PRS, resource repetition within an SRS occasion is not supported. In the time domain, a SRS resource may be transmitted when the following condition is fulfilled

$$\left(N_{\text{slot}}^{\text{frame},\mu} n_{\text{f}} + n_{\text{s,f}}^{\mu} - T_{\text{offset}}^{\text{SRS}}\right) \mod T_{\text{per}}^{\text{SRS}} = 0 \quad (8)$$

where $T_{\text{offset}}^{\text{SRS}}$ is the SRS resource offset and $T_{\text{per}}^{\text{SRS}}$ the SRS periodicity in time slots. SRS slot offset and periodicity, as well as all other parameters, are configured by the network via the radio resource control protocol as detailed in [56].

C. TOA Estimation

All time-based measurements carried out by the 5G network for localization purposes, i.e., time-difference-of-arrival (TDOA) (both DL-TDOA and UL-TDOA) and MRTT, are obtained by estimating the time-of-arrival (TOA) of specific RSs. For DL-TDOA measurements, the UE estimates the TOA of multiple PRS transmissions from neighbor gNBs, then the TOA relative to a reference gNB is subtracted from the other estimates. UL-TDOA measurements are obtained in a similar way, but in this case the TOA estimation is carried out at the gNB-side based on the SRS transmitted by the UE to be localized. On the other hand, MRTT measurements are obtained based on the TOA estimates from PRS and SRS.

In order to obtain the TOA, the UE or gNB estimates the delay of the first path of the channel impulse response based on the received RS $r(t)$. For example, this can be accomplished by evaluating the cross-correlation between the transmitted and received RS. Let $r[n] = r(nT_{\text{s}})$ denote a realization of the sampled version of the received signal $r(t)$ with sampling time T_{s}.[4] The cross-correlation $R_{r,s}[n]$ is defined as

$$R_{r,s}[n] = \sum_{j=0}^{N_{\text{samp}}-1} r[j] s^*[j-n] \quad (9)$$

for $n = 0, 1, \ldots, N_{\text{samp}}$, where $s[n] = s(nT_{\text{s}})$ and N_{samp} the number of RS samples. In line-of-sight (LOS) condition, the delay of the first channel path can reliably be estimated by searching for the strongest peak in the cross-correlation. However, in NLOS condition, the first channel path (LOS component of the received signal) is usually weak and the strongest peak in cross-correlation may represent late replicas of the transmitted signal, reaching the receiver via longer propagation paths, thus introducing a bias in the TOA estimate [57], [58], [59]. In order to mitigate this detrimental effect, iterative methods aimed at estimating the channel impulse response and consequently the first path, can be employed [60]. In each iteration, the strongest peak in $R_{r,s}[n]$ is identified and then its contribution is removed. Let $R_{r,s}^{(i)}[n]$ denote the cross-correlation at the i-th iteration. The discrete cross-correlation at iteration $i+1$ is obtained as

$$R_{r,s}^{(i+1)}[n] = R_{r,s}^{(i)}[n] - R_{r,s}^{(i)}[n^{(i)}] R_{s,s}[n - n^{(i)}] \quad (10)$$

where $n^{(i)} = \text{argmax}_n \left\{ R_{r,s}^{(i)}[n] \right\}$ and $R_{s,s}[n]$ is the normalized auto-correlation of the transmitted signal $s(t)$. At the iteration 0, the algorithm is initialized such that $R_{r,s}^{(0)}[n] = R_{r,s}[n]$. The algorithm stops after N_{I} iterations or when a specific criterion is met, such as the peak-to-average ratio falling below a certain threshold. Among the identified $N_{\text{I}}+1$ delays, $\{n^{(0)}, n^{(1)}, \ldots, n^{(N_{\text{I}})}\}$, the minimum is taken as estimated sample delay, i.e.,

$$\hat{n} = \min \left\{ n^{(0)}, n^{(1)}, \ldots, n^{(N_{\text{I}})} \right\} \quad (11)$$

and the estimated TOA is then obtained as $\hat{\tau} = \hat{n} T_{\text{s}}$. To increase the accuracy of the TOA estimates, cross-correlations obtained from different RS occasions can be coherently accumulated for increasing the signal-to-noise ratio (SNR).

D. AOD Estimation

In FR2, angle-based measurements are obtained by relying on the high number of antenna elements available at the gNB side [44], [45]. In particular, multiple PRS resources are transmitted by the gNB applying different steering vectors to the transmitting antenna array. The AOD is estimated by evaluating the received power levels at the UE side. The angle corresponding to the steering vector that determines the highest received power or SNR at the UE side is considered as the AOD estimate [45]. Consider azimuth AOD estimation and a single gNB serving an angular sector of A degrees. Denote with N_{A} the number of steering vectors related to different azimuth angles $\alpha^{(n)} = n\alpha_{\text{RES}}$ where $n \in \mathcal{N}_{\text{A}} = \{1, 2, \ldots, N_{\text{A}}\}$ and $\alpha_{\text{RES}} = \frac{A}{N_{\text{A}}}$ represents the angular resolution. Given the transmission of N_{A} PRS resources, where the n-th PRS resource is transmitted employing the n-th steering vector, the UE evaluates the SNR $\rho_{\text{A}}^{(n)}$ corresponding to the n-th PRS resource. Considering a realization of the SNR values, a first coarse AOD estimate is given by $\breve{\alpha} = \alpha^{(\hat{n})}$ where

$$\hat{n} = \underset{n \in \mathcal{N}_{\text{A}}}{\text{argmax}} \, \rho_{\text{A}}^{(n)} . \quad (12)$$

The estimate $\breve{\alpha}$ can be further refined considering the set of pairs $\{(\alpha^{(n)}, \rho_{\text{A}}^{(n)})\}_{n \in \mathcal{N}_{\text{A}}}$ [45]. For example, denote with $\rho_{\text{A}}^{(\hat{n}-1)}$ and $\rho_{\text{A}}^{(\hat{n}+1)}$ the SNRs associated to the angles $\alpha^{(\hat{n}-1)}$ and $\alpha^{(\hat{n}+1)}$, respectively. A refined AOD estimate $\hat{\alpha}$ can be

[4]The sampling time T_{s} is inversely proportional to the RS bandwidth.

obtained as weighted average of adjacent angles[5]

$$\hat{\alpha} = -\frac{\rho_{\mathrm{A}}^{(\hat{n}-1)}}{\rho_{\mathrm{A}}^{(\hat{n})}}\alpha_{\mathrm{RES}} + \breve{\alpha} + \frac{\rho_{\mathrm{A}}^{(\hat{n}+1)}}{\rho_{\mathrm{A}}^{(\hat{n})}}\alpha_{\mathrm{RES}}\,. \tag{13}$$

The number of steering vectors used for PRS transmission depends on the specific carrier frequency considered and the number of available antenna elements [38].

III. 5G Location Estimation

Existing 5G localization methods rely on SVEs using measurements described in Sec. II, namely TDOA, MRTT, and AOD. In general, SVE-based localization methods divide the localization process into two stages. In the first stage, a measurement vector $\boldsymbol{y}_i$ is defined as a collection of measurements obtained by the exchange with the i-th gNB, where $i \in \mathcal{N}_{\mathrm{bs}} = \{1, 2, \ldots, N_{\mathrm{bs}}\}$. For example, $\boldsymbol{y}_i$ can include the entire set of waveform samples, time-based, angle-based, and power-based metrics, or any combination of them. These measurements are related to a positional feature $\theta_i(\boldsymbol{p})$ which is a function of the UE position $\boldsymbol{p} \in \mathbb{R}^2$ and the position $\boldsymbol{p}_i^{\mathrm{BS}}$ of the i-th gNB. In the first stage of SVE-based localization methods, the measurements $\{\boldsymbol{y}_i\}_{i\in\mathcal{N}_{\mathrm{bs}}}$ are processed in order to obtain SVEs of the positional features, i.e., $\{\hat{\theta}_i\}_{i\in\mathcal{N}_{\mathrm{bs}}}$, such as distance or angle estimates. In the second stage, $\{\hat{\theta}_i\}_{i\in\mathcal{N}_{\mathrm{bs}}}$ are used as input to the localization algorithm to obtain an estimate of the UE position $\hat{\boldsymbol{p}}$.

In cellular localization, weighted least squares (WLS) is widely adopted for obtaining an estimate of the UE position $\hat{\boldsymbol{p}}$ given a particular set of SVEs $\{\hat{\theta}_i\}_{i\in\mathcal{N}_{\mathrm{bs}}}$ [61], [62], [63]. In particular, WLS assumes the following measurement model

$$\hat{\boldsymbol{\theta}} = \boldsymbol{\theta}(\boldsymbol{p}) + \mathbf{w} \tag{14}$$

where

$$\hat{\boldsymbol{\theta}} = \left[\hat{\theta}_1, \hat{\theta}_2, \ldots, \hat{\theta}_{N_{\mathrm{bs}}}\right]^{\mathrm{T}} \tag{15a}$$

$$\boldsymbol{\theta}(\boldsymbol{p}) = \left[\theta_1(\boldsymbol{p}), \theta_2(\boldsymbol{p}), \ldots, \theta_{N_{\mathrm{bs}}}(\boldsymbol{p})\right]^{\mathrm{T}} \tag{15b}$$

$$\mathbf{w} = \left[\mathsf{w}_1, \mathsf{w}_2, \ldots, \mathsf{w}_{N_{\mathrm{bs}}}\right]^{\mathrm{T}} \tag{15c}$$

with $\mathbf{w}$ denoting a zero-mean Gaussian noise vector with covariance matrix $\boldsymbol{\Sigma} = \mathbb{E}\{\mathbf{w}\mathbf{w}^{\mathrm{T}}\}$. Given a realization of the SVE vector $\hat{\boldsymbol{\theta}}$, the UE estimated position is obtained as

$$\hat{\boldsymbol{p}} = \underset{\tilde{\boldsymbol{p}}}{\operatorname{argmin}} \left(\hat{\boldsymbol{\theta}} - \boldsymbol{\theta}(\tilde{\boldsymbol{p}})\right)^{\mathrm{T}} \boldsymbol{\Sigma}^{-1} \left(\hat{\boldsymbol{\theta}} - \boldsymbol{\theta}(\tilde{\boldsymbol{p}})\right). \tag{16}$$

Depending on the functional form of $\theta_i(\boldsymbol{p})$, a solution to (16) can be obtained either in closed form, employing gradient-free optimization algorithms such as grid search, random search, or particle swarm optimization [64], or employing gradient-based optimization algorithms using a simplified cost function such as Levenberg–Marquardt algorithm [61].

WLS approach can be modified to exploit heterogeneous measurements [65], [66]. In particular, consider N_{F} different SVEs $\hat{\theta}_i^{(j)}$ with $i \in \mathcal{N}_{\mathrm{bs}}$ and $j \in \mathcal{N}_{\mathrm{F}} = \{1, 2, \ldots, N_{\mathrm{F}}\}$ obtained from N_{F} types of sensors and define

$$\breve{\boldsymbol{\theta}}^{(j)} = \left[\hat{\theta}_1^{(j)}, \hat{\theta}_2^{(j)}, \ldots, \hat{\theta}_{N_{\mathrm{bs}}}^{(j)}\right] \tag{17a}$$

$$\breve{\boldsymbol{\theta}}^{(j)}(\boldsymbol{p}) = \left[\theta_1^{(j)}(\boldsymbol{p}), \theta_2^{(j)}(\boldsymbol{p}), \ldots, \theta_{N_{\mathrm{bs}}}^{(j)}(\boldsymbol{p})\right] \tag{17b}$$

$$\breve{\mathbf{w}}^{(j)} = \left[\mathsf{w}_1^{(j)}, \mathsf{w}_2^{(j)}, \ldots, \mathsf{w}_{N_{\mathrm{bs}}}^{(j)}\right]. \tag{17c}$$

Then, the UE position estimate can be obtained via (16) considering

$$\hat{\boldsymbol{\theta}} = \left[\breve{\boldsymbol{\theta}}^{(1)}, \breve{\boldsymbol{\theta}}^{(2)}, \ldots, \breve{\boldsymbol{\theta}}^{(N_{\mathrm{F}})}\right]^{\mathrm{T}} \tag{18a}$$

$$\boldsymbol{\theta}(\boldsymbol{p}) = \left[\breve{\boldsymbol{\theta}}^{(1)}(\boldsymbol{p}), \breve{\boldsymbol{\theta}}^{(2)}(\boldsymbol{p}), \ldots, \breve{\boldsymbol{\theta}}^{(N_{\mathrm{F}})}(\boldsymbol{p})\right]^{\mathrm{T}} \tag{18b}$$

$$\mathbf{w} = \left[\breve{\mathbf{w}}^{(1)}, \breve{\mathbf{w}}^{(2)}, \ldots, \breve{\mathbf{w}}^{(N_{\mathrm{F}})}\right]^{\mathrm{T}}. \tag{18c}$$

1) TDOA Measurements: consider N_{bs} gNBs providing TDOA measurements with respect to an additional gNB used as reference gNB indexed by 0. Denote the TDOA measurements obtained from the i-th neighbor gNB and the reference gNB with

$$\hat{\tau}_{i,0} = \hat{\tau}_i - \hat{\tau}_0 \tag{19}$$

where $i \in \mathcal{N}_{\mathrm{bs}}$, $\hat{\tau}_i$ is the TOA estimate relative to the i-th gNB and $\hat{\tau}_0$ is the TOA estimate relative to the reference gNB obtained from the PRS or SRS for downlink or uplink transmission, respectively. In this case, the vector elements in (15a) and (15b) can be written as

$$\begin{aligned}\hat{\theta}_i &= c\,\hat{\tau}_{i,0} \\ &= \hat{\mathsf{d}}_{i,0}\end{aligned} \tag{20a}$$

$$\begin{aligned}\theta_i(\boldsymbol{p}) &= d_{i,0}(\boldsymbol{p}) \\ &= d_i(\boldsymbol{p}) - d_0(\boldsymbol{p})\end{aligned} \tag{20b}$$

where $d_i(\boldsymbol{p}) = \left|\left|\boldsymbol{p} - \boldsymbol{p}_i^{\mathrm{BS}}\right|\right|_2$, $d_0(\boldsymbol{p}) = \left|\left|\boldsymbol{p} - \boldsymbol{p}_0^{\mathrm{BS}}\right|\right|_2$, $i \in \mathcal{N}_{\mathrm{bs}}$, c is the signal propagation speed and $\boldsymbol{p}_0^{\mathrm{BS}}$ denotes the coordinates of the reference gNB.

2) MRTT Measurements: for MRTT-based localization, the problem formulation is similar to what presented for TDOA-based localization, with a few differences in the measurement model. Given N_{bs} gNBs, the network estimates N_{bs} round-trip time (RTT) measurements defined as[6]

$$\hat{\tau}_i = \frac{1}{2}(\hat{\tau}_i^{\mathrm{PRS}} + \hat{\tau}_i^{\mathrm{SRS}}) \tag{21}$$

where $\hat{\tau}_i^{\mathrm{PRS}}$ and $\hat{\tau}_i^{\mathrm{SRS}}$ are the TOA estimates obtained from the PRS and SRS, respectively. Then, the measurement model in (15a) and (15b) is modified as

$$\begin{aligned}\hat{\theta}_i &= c\,\hat{\tau}_i \\ &= \hat{\mathsf{d}}_i\end{aligned} \tag{22a}$$

$$\theta_i(\boldsymbol{p}) = d_i(\boldsymbol{p}) \tag{22b}$$

where $i \in \mathcal{N}_{\mathrm{bs}}$ and $d_i(\boldsymbol{p})$ is defined in (20).

[5]The weighted average can be expanded to include other angles and power measurements in addition to the adjacent ones.

[6]The processing delays of the RSs at the UE are neglected for simplicity.

3) AOD Measurements: for AOD-based localization, measurement model in (15a) and (15b) can be written as

$$\hat{\theta}_i = \hat{\alpha}_i \tag{23a}$$

$$\theta_i(\boldsymbol{p}) = \alpha_i(\boldsymbol{p}) \tag{23b}$$

where $i \in \mathcal{N}_{\text{bs}}$ and $\alpha_i(\boldsymbol{p})$ represents the azimuth angle between the i-th gNB and the position $\boldsymbol{p}$.

IV. SI for 5G and Beyond Localization

SI has been proposed in [46] and is developed here to overcome the limitations of SVE-based localization in 5G and beyond networks. SI encapsulates all the positional information of the UE associated with the sensing measurements and the contextual data. In particular, the ensemble of positional information associated with the measurements is referred to as soft feature information (SFI). SFI provides a statistical characterization of the relationship between the sensing measurements and positional features. This is represented by a measurement vector $\boldsymbol{y}_i$ and a feature vector $\boldsymbol{\theta}_i$ function of the UE positional state such as UE position, velocity, and bearing with $i \in \mathcal{N}_{\text{bs}}$. On the other hand, the ensemble of positional information associated with the contextual data (e.g., digital map and mobility model) is referred to as soft context information (SCI).[7] SI-based localization leverages both SFI and SCI to infer the UE position $\hat{\boldsymbol{p}}$.

In current 5G localization architecture, the measurement vectors $\boldsymbol{y}_i$ are not directly available to the network, and only SVEs $\hat{\theta}_i$ are exploited for localization purposes [67], [68]. In order to leverage the strengths of SI-based localization in 5G networks without requiring a complete redesign of the localization protocols and architecture, we propose to extract the SFI directly from the SVEs. In particular, at the UE side, the SI-based localization process is identical to the SVE-based process described in Sec. III. However, this approach can easily be adapted to take into account new types of measurements that might be available in future beyond 5G networks. In particular, SFI can be extracted from any combination of SVEs and other possible metrics.

A. SFI Based on 5G Measurements

In this section, SFI is specialized taking into account the measurement capabilities of current 5G networks. In particular, the measurement vector is given by the SVE associated to a RAT-dependent measurement ($\boldsymbol{y}_i = \hat{\theta}_i$) and the feature vector is given by the actual value of the feature associated to the SVE ($\boldsymbol{\theta}_i = \theta_i$). Thus, the SFI related to the feature θ and its SVE $\hat{\theta}$ is

$$\mathcal{L}_{\hat{\theta}}(\theta) \propto f_{\hat{\theta}}(\hat{\theta};\theta) \tag{24}$$

where the non-Bayesian formulation has been reported. In the non-Bayesian formulation, the SFI is equivalent to the likelihood function of θ. Compared to the single SVE $\hat{\theta}$, the SFI $\mathcal{L}_{\hat{\theta}}(\theta)$ provides richer information by accounting probabilistically for all possible values of θ, thus enabling soft-decision localization instead of hard-decision. Depending on the specific SVE, different types of SFI are obtained. For range-related estimates, the corresponding SFI, namely soft range information (SRI), can be written as $\mathcal{L}_{\hat{\theta}}(d)$. Similarly, the soft angle information (SAI) $\mathcal{L}_{\hat{\theta}}(\alpha)$ is defined for angle-related measurements.

Considering that the measurements from different gNBs given the UE location are statistically independent, the UE position $\boldsymbol{p}$ can be estimated via the maximum likelihood (ML) estimation exploiting the SFI as

$$\begin{aligned}\hat{\boldsymbol{p}} &= \underset{\tilde{\boldsymbol{p}}}{\operatorname{argmax}}\, f(\{\hat{\theta}_i\}_{i\in\mathcal{N}_{\text{bs}}};\tilde{\boldsymbol{p}}) \\ &= \underset{\tilde{\boldsymbol{p}}}{\operatorname{argmax}} \prod_{i\in\mathcal{N}_{\text{bs}}} \mathcal{L}_{\hat{\theta}_i}(\theta_i)\,.\end{aligned} \tag{25}$$

As an example, consider DL-TDOA measurements obtained from 5G PRS. In this setting, recalling (20), the SRI can be written as $\mathcal{L}_{\hat{d}_{i,0}}(d_{i,0})$. Analogously from (22) and (23), SRI and SAI related to MRTT and AOD measurements are given by $\mathcal{L}_{\hat{d}_i}(d_i)$ and $\mathcal{L}_{\hat{\alpha}_i}(\alpha_i)$, respectively. Similarly to WLS presented in Sec. III, (25) can be solved with gradient-free optimization methods such as grid search and random search, or particle swarm optimization [64].

The SI-based approach enables efficient data fusion. In particular, SVEs obtained from heterogeneous measurements can be fused by multiplying their corresponding SFI, as long as the measurements are conditionally independent given the UE position. If such conditions are satisfied, given a set of SVEs $\hat{\Theta}_i = \{\hat{\theta}_i^{(j)}\}_{j\in\mathcal{N}_{\text{F}}}$ related to the feature set $\Theta_i = \{\theta_i^{(j)}\}_{j\in\mathcal{N}_{\text{F}}}$, the SFI is given by

$$\mathcal{L}_{\hat{\Theta}_i}(\Theta_i) = \prod_{j\in\mathcal{N}_{\text{F}}} \mathcal{L}_{\hat{\theta}_i^{(j)}}(\theta_i^{(j)})\,. \tag{26}$$

As an example, consider the fusion of DL-TDOA and AOD measurements. In this setting, the resulting SFI obtained by the fusion of SRI and SAI can be written as

$$\mathcal{L}_{\hat{\Theta}_i}(\Theta_i) = \mathcal{L}_{\hat{d}_{i,0}}(d_{i,0})\,\mathcal{L}_{\hat{\alpha}_i}(\alpha_i)\,. \tag{27}$$

Fig. 3 depicts a pictorial representation of the SFI obtained from the fusion of the SRI extracted from DL-TDOA measurements (relative to the gNBs 1 and 2, considering the gNB 0 as reference) and the SAI extracted from AOD measurements (relative to gNB 0). Intensity of SRI is shown with a red-yellow colormap, while the intensity of SAI is shown with a green colormap. The total SFI obtained as multiplication of the SRI and SAI is shown with a blue colormap. Lighter colors are associated to higher values of SFI.

B. SFI Learning

SFI can be determined using a Bayesian framework, and in particular leveraging the joint probability distribution of $\hat{\theta}$ and θ, referred to as generative model.[8] In the absence of prior

[7]The exploitation of SCI and its generation is not directly related to the specific technology employed. For brevity, we also dropped the dependency of $\boldsymbol{\theta}_i$ on the position $\boldsymbol{p}$.

[8]SFI can be leveraged to perform localization considering both a non-Bayesian or a Bayesian formulation of the interference problem. However, in order to learn the statistical relationship between the measurement vector and feature vector, it is convenient to consider the feature vector as a random quantity.

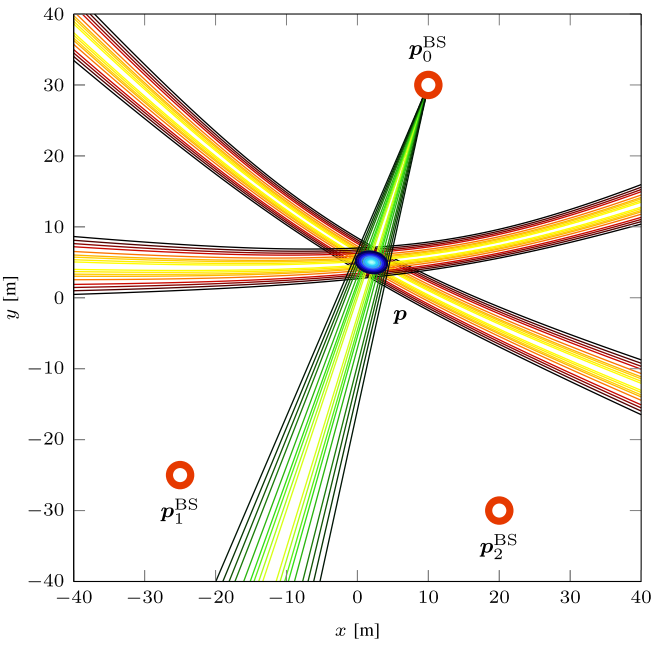

Fig. 3. SRI based on DL-TDOA measurements obtained from gNBs 1 and 2, considering the gNB 0 as reference (represented by red annolous), and SAI based on AOD measurements obtained from gNB 0. Lighter colors correspond to SFI higher values.

information on the feature θ, the SFI is determined by

$$\mathcal{L}_{\hat{\theta}}(\theta) \propto f_{\hat{\theta},\theta}(\hat{\theta},\theta)\,. \tag{28}$$

Thus, the task of determining the SFI is equivalent to the task of determining the generative model relating the SVE with its true value. In complex scenarios, this can be accomplished by employing unsupervised machine learning techniques applied to measurements and positional feature data acquired in the scenario of interest. In particular, a two-phase algorithm is used to estimate the generative model based on density estimation techniques. The algorithm works as follows: i) an off-line phase where a generative model estimate is obtained from the SVEs and their true values; and ii) an on-line phase where the generative model estimate is used to determine the SFI associated with each new SVE.

In the following, a density estimation technique used for determining the generative model is presented. Such density estimation technique considers as generative model a Gaussian mixture (GM) model [69]. For notational convenience, consider the vector $\boldsymbol{x} = [\hat{\theta},\theta]^{\mathrm{T}}$. In this case, the generative model to be estimated is $f(\boldsymbol{x}) = f(\hat{\theta},\theta)$. Prior to the density estimation process, it is beneficial to pre-process the data and normalize the different variables via data-sphering [70]. Data sphering is a linear transformation that maps the original data into a set with mean zero and identity covariance matrix. Let $\{\tilde{\boldsymbol{x}}_{i,n^{(i)}}\}_{n^{(i)}\in\mathcal{N}_{\mathrm{t}}^{(i)}}$ be the set of unprocessed data, where

$$\mathcal{N}_{\mathrm{t}}^{(i)} = \left\{1,2,\ldots,N_{\mathrm{t}}^{(i)}\right\} \tag{29}$$

and $N_{\mathrm{t}}^{(i)}$ is the number of training points relative to the i-th gNB. For notation brevity, define $\boldsymbol{x}_l = \tilde{\boldsymbol{x}}_{i,n^{(i)}}$ where $l =: N_{\mathrm{t}}^{(i)}(i-1)+n^{(i)}$ and $l \in \mathcal{N}_{\mathrm{t}} = \{1,2,\ldots,N_{\mathrm{t}}\}$ with $N_{\mathrm{t}} = \sum_{i\in\mathcal{N}_{\mathrm{bs}}} N_{\mathrm{t}}^{(i)}$. Then, the processed data after sphering are given by

$$\boldsymbol{z}_l = \boldsymbol{\Lambda}^{-\frac{1}{2}}\boldsymbol{U}^{\mathrm{T}}(\boldsymbol{x}_l - \bar{\boldsymbol{x}}) \tag{30}$$

where $\bar{\boldsymbol{x}}$ is the sample mean of the unprocessed data, and $\boldsymbol{U}\boldsymbol{\Lambda}\boldsymbol{U}^{\mathrm{T}}$ is the spectral decomposition of the sample covariance matrix of the unprocessed data $\{\boldsymbol{x}_l\}_{l\in\mathcal{N}_{\mathrm{t}}}$.[9] Then, the estimated density of the non-sphered data $\hat{f}_{\mathbf{x}}(\boldsymbol{x})$ can be obtained from the estimated density $\hat{f}_{\mathbf{z}}(\boldsymbol{z})$ as follows

$$\begin{aligned}\hat{f}_{\mathbf{x}}(\boldsymbol{x}) &= \left|\det(\boldsymbol{\Lambda}^{-\frac{1}{2}}\boldsymbol{U}^{\mathrm{T}})\right|\ \hat{f}_{\mathbf{z}}(\boldsymbol{z}) \\ &= \left|\det(\boldsymbol{\Lambda}^{-\frac{1}{2}}\boldsymbol{U}^{\mathrm{T}})\right|\ \hat{f}_{\mathbf{z}}(\boldsymbol{\Lambda}^{-\frac{1}{2}}\boldsymbol{U}^{\mathrm{T}}(\boldsymbol{x}-\bar{\boldsymbol{x}}))\,.\end{aligned} \tag{31}$$

Assume that the sphered data $\{\boldsymbol{z}_l\}_{l\in\mathcal{N}_{\mathrm{t}}}$ are realizations of independent, identically distributed random variables (RVs) following a GM distribution given by

$$\tilde{f}(\boldsymbol{z};\mathcal{P}) = \sum_{k\in\mathcal{N}_{\mathrm{G}}} \pi_k \varphi(\boldsymbol{z};\boldsymbol{\mu}_k,\boldsymbol{\Sigma}_k) \tag{32}$$

where $\mathcal{N}_{\mathrm{G}} = \{1,2,\ldots,N_{\mathrm{G}}\}$, N_{G} is the number of Gaussian components forming the mixture, and $\pi_k \in \mathbb{R}^+$ with $\sum_{k\in\mathcal{N}_{\mathrm{G}}}\pi_k = 1$ represents the weight of the k-th Gaussian component. The set of parameters $\mathcal{P} = \{\pi_k,\boldsymbol{\mu}_k,\boldsymbol{\Sigma}_k\}_{k\in\mathcal{N}_{\mathrm{G}}}$ along with N_{G} completely define the distribution. Therefore, the problem of obtaining the estimate $\hat{f}(\boldsymbol{z})$ is equivalent to the problem of determining the optimum set of parameters $\hat{\mathcal{P}}$ which describe the sphered data $\{\boldsymbol{z}_l\}_{l\in\mathcal{N}_{\mathrm{t}}}$, i.e., $\hat{f}(\boldsymbol{z}) = \tilde{f}(\boldsymbol{z};\hat{\mathcal{P}})$. This problem can be solved by applying a ML approach, and in particular, given the independent, identically distributed assumption, the log-likelihood function can be written as

$$\begin{aligned}\Lambda\big(\{\boldsymbol{z}_l\}_{l\in\mathcal{N}_{\mathrm{t}}};\mathcal{P}\big) &= \ln\left\{\tilde{f}(\{\boldsymbol{z}_l\}_{l\in\mathcal{N}_{\mathrm{t}}};\mathcal{P})\right\} \\ &= \sum_{l\in\mathcal{N}_{\mathrm{t}}} \ln\left\{\sum_{k\in\mathcal{N}_{\mathrm{G}}} \pi_i\varphi(\boldsymbol{z}_l;\boldsymbol{\mu}_k,\boldsymbol{\Sigma}_k)\right\}\end{aligned} \tag{33}$$

and the optimal set of parameters $\hat{\mathcal{P}}$ is obtained by maximizing (33), i.e.,

$$\hat{\mathcal{P}} = \underset{\mathcal{P}}{\operatorname{argmax}} \sum_{l\in\mathcal{N}_{\mathrm{t}}} \ln\left\{\sum_{k\in\mathcal{N}_{\mathrm{G}}} \pi_i\varphi(\boldsymbol{z}_l;\boldsymbol{\mu}_k,\boldsymbol{\Sigma}_k)\right\} \tag{34}$$

Note that no closed-form solution can be obtained for (34). Therefore, iterative algorithms are employed to determine an approximate ML solution. The expectation-maximization (EM) algorithm is typically used to solve (34) [69] which consists of the following steps:

1) At the first iteration for $n = 0$, initialize the set parameter $\hat{\mathcal{P}}^{[0]}$ by performing clustering on the data $\{\boldsymbol{z}_l\}_{l\in\mathcal{N}_{\mathrm{t}}}$, for example via k-means algorithm [71], with the number of clusters equal to the number N_{G} of components in the GM model. The parameters π_k are calculated as the fraction of data $\boldsymbol{z}_l^{[0]}$ assigned to the k-th cluster, while $\boldsymbol{\mu}_k^{[0]}$ and $\boldsymbol{\Sigma}_k^{[0]}$ are calculated as the sample mean and

[9] $\boldsymbol{\Lambda}$ is a diagonal matrix where the diagonal elements are given by the eigenvalues of the empirical covariance matrix corresponding to the eigenvectors that are the columns of $\boldsymbol{U}$.

sample covariance of the data $\boldsymbol{z}_l$ assigned to the k-th cluster, respectively.

2) for n increasing, starting from the current values of the parameters, calculate:

$$\gamma_{k,l}^{[n]} = \pi_k^{[n]} \frac{\varphi(\boldsymbol{z}_l; \boldsymbol{\mu}_k^{[n]}, \boldsymbol{\Sigma}_k^{[n]})}{\tilde{f}(\boldsymbol{z}_l; \hat{\mathcal{P}}^{[n]})} \tag{35a}$$

$$\Gamma_k^{[n]} = \sum_{l \in \mathcal{N}_\mathrm{t}} \gamma_{k,l}^{[n]} . \tag{35b}$$

3) Update the weights, mean vectors and covariance matrices as follows

$$\pi_k^{[n+1]} = \frac{\Gamma_k^{[n]}}{N_\mathrm{t}} \tag{36a}$$

$$\boldsymbol{\mu}_k^{[n+1]} = \frac{1}{\Gamma_k^{[n]}} \sum_{l \in \mathcal{N}_\mathrm{t}} \gamma_{k,l}^{[n]} \boldsymbol{z}_l \tag{36b}$$

$$\boldsymbol{\Sigma}_k^{[n+1]} = \frac{1}{\Gamma_k^{[n]}} \sum_{l \in \mathcal{N}_\mathrm{t}} \gamma_{k,l}^{[n]} (\boldsymbol{z}_l - \boldsymbol{\mu}_k^{[n+1]})(\boldsymbol{z}_l - \boldsymbol{\mu}_k^{[n+1]})^\mathrm{T} . \tag{36c}$$

4) Evaluate the log-likelihood function (33) with the new parameters (36) and check for convergence of the log-likelihood, i.e.,

$$\Lambda\big(\{\boldsymbol{z}_l\}_{l \in \mathcal{N}_\mathrm{t}}; \hat{\mathcal{P}}^{[n+1]}\big) \leqslant \Lambda\big(\{\boldsymbol{z}_l\}_{l \in \mathcal{N}_\mathrm{t}}; \hat{\mathcal{P}}^{[n]}\big) + \epsilon_\mathrm{th} \tag{37}$$

where $\epsilon_\mathrm{th} > 0$ is a predefined threshold.[10] If convergence is not achieved, repeat from 2).

The EM algorithm is widely employed GM model fitting due to its simplicity and flexibility. However, EM may converge to a local maximum instead of a global maximum. Moreover, the convergence rate strongly depends on the initialization parameters. Multiple runs of EM can be performed with different initialization parameters, and we keep the solution with the highest log-likelihood value. In particular, the initial centroids of the k-means algorithm can be selected randomly for each run, thus determining different values of $\hat{\mathcal{P}}^{[0]}$. The number of runs required to achieve a satisfactory fitting of the GM depends on the data set considered.

Density estimation via the GM model produces a parsimonious generative model characterized by a small number of parameters π_k, $\boldsymbol{\mu}_k$, and $\boldsymbol{\Sigma}_k$ for $k \in \mathcal{N}_\mathrm{G}$ where the only free parameter is the number of components in the GM N_G. However, generative models with a fixed number of parameters may not be suitable for capturing complex relations between the measurement and feature vectors. In this case, cross-validation procedures can be employed to determine the optimal or near-optimal value of N_G for the performance metric under consideration [72].

V. Case Studies

This section presents the results on SI-based localization in two 3GPP standardized scenarios. The results are obtained using the SI-based algorithm presented in the previous section and using a 5G localization simulator developed in conformity with 3GPP technical reports and technical specifications [38], [44], [54], [55].

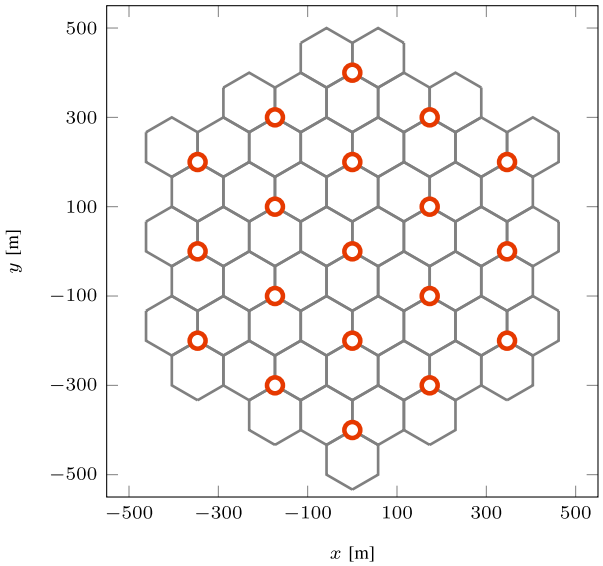

(a) UMi site spatial displacement with 19 sites (3 sectors per site).

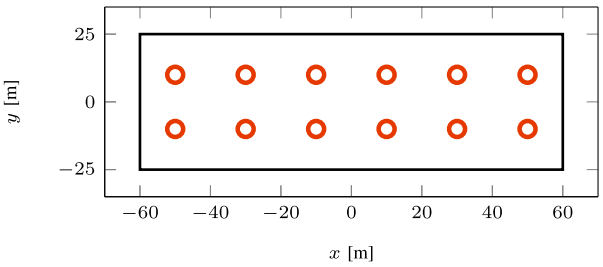

(b) IOO site spatial displacement with 12 sites (1 sector per site).

Fig. 4. Site spatial displacement (red annuluses) for the two scenarios under consideration.

Among the different 5G scenarios considered in [38], we provide results for both IOO and UMi scenarios. The IOO scenario is characterized by a higher probability of LOS links, while UMi scenario represents a harsher wireless propagation environment, with higher delay spreads and probability of NLOS links.[11] In each scenario, different channel models, number of sites, spatial displacement of the site, inter-site distance, and number of sectors per site (i.e., number of gNBs per site) are considered. Fig. 4 depicts the spatial deployment of the sites and their relative sectors for the two scenarios.

In [38] different carrier frequency and numerologies for 5G localization are specified. In particular, for FR1 the carrier frequencies of 2 GHz and 4 GHz, with numerologies $\mu = 0$ and $\mu = 1$ (15 kHz and 30 kHz of SC spacing) are considered, respectively. For FR2 the carrier frequency of 30 GHz with a numerology $\mu = 3$ (120 kHz of SC spacing) is considered as representative. Different antenna arrays for UEs and gNB, receiver noise figure, and transmitted power are specified for each scenario [38], [43], [73]. For IOO, the simulator is capable of simulating a 5G localization system based on

[10] Recall that the log-likelihood function value increases at each iteration.

[11] For a UE deployed uniformly at random in the considered environment, the probability of having at least three gNBs in LOS condition is approximately 99% and 15% for IOO and UMi scenarios, respectively.

TABLE II
COMMON SIMULATION PARAMETERS FOR THE TWO SCENARIOS UNDER CONSIDERATION

Parameter	FR1 Value		FR2 Value
Configuration Name	Type I	Type II	Type III
Carrier Frequency	2 GHz	4 GHz	30 GHz
SC Spacing	15 kHz	30 kHz	120 kHz
RSs Bandwidth	50 MHz	100 MHz	400 MHz
gNB Noise Figure	5 dB		7 dB
UE TX Power	23 dBm		
UE EIRP Limit	-		43 dBm
UE Noise Figure	9 dB		13 dB
UE Antenna Configuration	4 (2 per polarization)		See TR 38.855 [38]
UE Antenna Elem. Radiation Pattern	Omni (0 dBi)		See TR 38.855 [38]
UE Antenna Height	1.5 m		

TABLE III
SCENARIO-SPECIFIC SIMULATION PARAMETERS ACCORDING TO 3GPP SPECIFICATIONS

Parameter	UMi	IOO	
	FR1	FR1	FR2
Area	500 m × 500 m	120 m × 50 m	
Number of Sites	19	12	
Intersite Distance	200 m	20 m	
gNB Ant. Height	10 m	3 m	
Number of Sectors	3	1	3
gNB TX Power	44 dBm	24 dBm	
gNB EIRP Limit	-	-	58 dBm
gNB Antenna Elem. Radiation Pattern	See TR 38.802 [73] and TR 38.855 [38]		

DL-TDOA, UL-TDOA and MRTT measurements obtained by exploiting PRS and SRS in both FR1 and FR2. In addition, AOD measurements are considered in the case of FR2. Models and algorithms for both TOA estimation and AOD estimation are as described in Sec. III. Both PRS and SRS are fully compliant with the specifications contained in [54] and [55] including the allocation in the frequency domain (i.e., comb structure), the number of RBs, the number of symbols per occasion, and the periodicity of occasions as described in Sec. II. Results in terms of the empirical cumulative distribution function (ECDF) $\widetilde{P}(e_{\text{th}})$ for the horizontal localization error for existing 5G localization solutions based on SVE and for SI-based localization developed are presented in the IOO and UMi scenarios. In addition, the fusion of DL-TDOA and AOD measurements via both approaches are reported.

The channel is compliant with [51] and it is simulated using the Quadriga channel simulator [74], which includes spatially correlated large scale fading parameters. The gNBs antenna array configurations are taken as in [75], and perfect synchronization and ideal muting (i.e., no interference from neighbour gNBs) are considered for the simulations [38]. Recalling the quantities defined in Sec. II, both PRS and SRS have a comb size of 4 SCs, and each estimate is obtained using 3 RS occasions composed by 4 symbols. The RS occupies 272 RBs; it exhibits a bandwidth of 50 MHz and 100 MHz for the carrier frequency of 2 GHz and 4 GHz, respectively; and it exhibits a bandwidth of 400 MHz for the carrier frequency of 30 GHz. Tab. II summarizes the major simulation parameters common to the two scenarios, while Tab. III reports the simulation parameters specific for each scenario. The gNBs which perform TDOA, RTT, and AOD measurements are selected based on the SNR of the RSs. In particular, for TDOA measurements, the reference gNB is selected as the one with the highest RS SNR, while all gNBs that exhibit a RS SNR greater than -13 dB provides time- or angle-based measurements [76]. For time-based measurements, a vertical uniform linear array composed of 4 antenna elements per polarization is employed at the gNB side to transmit and receive the RSs [75]. Each antenna element has a maximum directional gain of 8 dBi and a half-power beamwidth of approximately 65° [38], [73]. TOA of the RSs is inferred using the iterative algorithm presented in Sec. II-C. TDOA and MRTT measurements are as presented in Sec. III-1 and Sec. III-2, respectively. AOD measurements based on PRS are obtained using an uniform rectangular array of 4×4 antenna elements per polarization. The number of employed steering vectors is $N_{\text{A}} = 10$ which determines an angular resolution of $\alpha_{\text{RES}} = 12^\circ$ considering an angular sector of $A = 120^\circ$. AOD estimation is performed using the algorithm as described in Sec. II-D and as per the measurement model presented in Sec. III-3.

For each combination of scenario and carrier frequency, 500 different instantiations of the wireless channel are simulated. Ten UEs are randomly placed in the environment following a bidimensional uniform distribution and are localized in each instantiation. Due to the spatial correlation of the large-scale and small-scale fading coefficients, each UE experiences a different wireless channel.[12] Performance for both SVE-based localization and SI-based localization are evaluated via a k-fold cross-validation technique with $k = 10$ [72]. Specifically, in the *training phase* (i.e., off-line phase) a subset of measurements is used for inferring: (i) the value of N_{I} in (11) which determines the lowest average ranging error for time-based measurements; (ii) the covariance matrix $\boldsymbol{\Sigma}$ for the WLS problem in (16); and (iii) the generative model used by the SI-based approach in (25). Then, the measurements not used in the off-line phase are used in the *validation phase* (i.e., on-line phase) to assess the localization performance of both SVE-based and SI-based approaches. A GM model with $N_{\text{G}} = 3$ components is assumed as generative model for the SFI considering a threshold $\epsilon_{\text{th}} = 10^{-9}$ in (37) [48]. For each type of measurement, five independent runs of the EM algorithm have been carried out considering randomly chosen centroids for the initialization of the k-means algorithm. The generative model associated with the highest log-likelihood value is used to perform SI-based localization. Each independent run of the EM algorithm uses 25000 measurements to fit the GM model.

[12]The number of measurements used to localize each UE varies from instantiation to instantiation and depends on the number of links that satisfy the condition on the RS SNR.

TABLE IV
ACCURACY OF DISTANCE ESTIMATE OBTAINED VIA TOA ESTIMATIONS AND ACCURACY OF AOD ESTIMATION

Scenario & Setting	SVE	RMSE	Med.	Std. Dev.	90-th Perc.
UMi Type I	DL DE	20.25 m	4.45 m	17.74 m	23.25 m
	UL DE	24.52 m	4.49 m	22.20 m	23.67 m
UMi Type II	DL DE	16.96 m	3.40 m	15.05 m	18.73 m
	UL DE	26.35 m	3.47 m	24.71 m	19.59 m
IOO Type I	DL DE	2.82 m	1.38 m	2.14 m	3.65 m
	UL DE	2.88 m	1.39 m	2.20 m	2.61 m
IOO Type II	DL DE	2.24 m	0.73 m	1.90 m	2.61 m
	UL DE	2.53 m	0.73 m	2.22 m	2.63 m
IOO Type III	DL DE	2.89 m	0.17 m	2.77 m	1.27 m
	UL DE	3.15 m	0.17 m	3.02 m	1.40 m
	AOD	51.08°	2.32°	49.75°	7.70°

The optimization in (16) and (25) is carried out via particle swarm optimization [64].[13]

In the following subsections, performance results for various scenarios and simulation settings are presented: (a) UMi Type I; (b) UMi Type II; (c) IOO Type I; (d) IOO Type II; and (e) IOO Type III. In Tab. II, the definition of Type I, Type II, and Type III simulation settings are reported. In Tab. IV accuracy of single-value estimation of the distances obtained from TOA measurements and angles obtained from AOD measurements is presented.[14] In the performance plots shown in Figs. 5–10, the dash-dotted lines represent the ECDF of SVE-based localization methods (i.e., WLS method) and the solid lines represent the ECDF of SI-based localization methods. Blue triangles, orange squares, green circles, violet diamonds and yellow asterisks denote the performance associated with DL-TDOA, UL-TDOA, MRTT, AOD, and fusion of DL-TDOA and AOD measurements, respectively. In addition, in Tab. V performance results for different values of the generative model parameters are presented for various settings. The convergence of the EM algorithm used to fit the generative models is also presented in Tab. VI.

A. Performance Results: Single-Value Estimates of Distance and Angle

Tab. IV reports the root-mean-square error (RMSE), median value, standard deviation, and 90-th percentile of the absolute error between the estimated and true value for the distances obtained from TOA measurements and angles obtained from AOD measurements. Distance estimate (DE) accuracy for both downlink and uplink is presented for all combinations of scenarios and simulation settings, while AOD estimate accuracy is reported for IOO Type III. It can be observed that DEs are significantly more accurate for IOO scenario compared to UMi scenario. For downlink DEs in IOO Type I settings, RMSE and median are approximately 20 m and 3 m lower compared to downlink DE in UMi Type I settings, respectively. This can be attributed to the fact that UMi scenario is a harsher wireless propagation environment with higher delay spread and higher probability of NLOS. It can also be noticed that uplink DE accuracy is slightly worse compared to downlink DE. This can be attributed to the lower transmission power of the SRS compared to the PRS. Focusing on AOD estimation, it can be noticed that despite the finite number of steering vectors employed to transmit the PRS, median and 90-th percentile are below 8°.

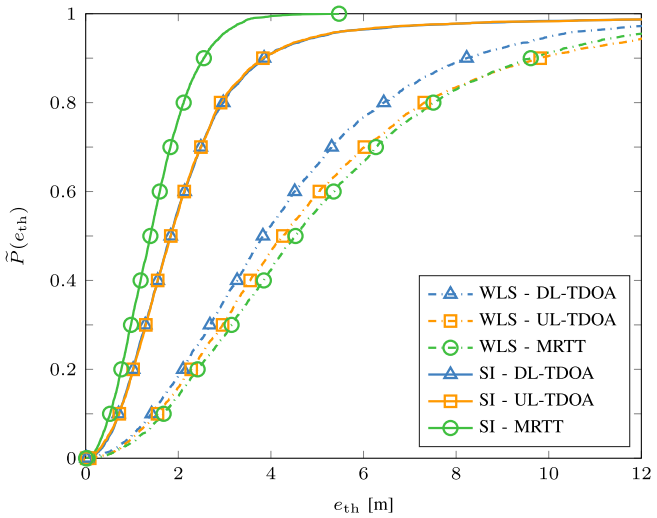

Fig. 5. ECDF for the horizontal localization error: UMi scenario and Type I simulation setting.

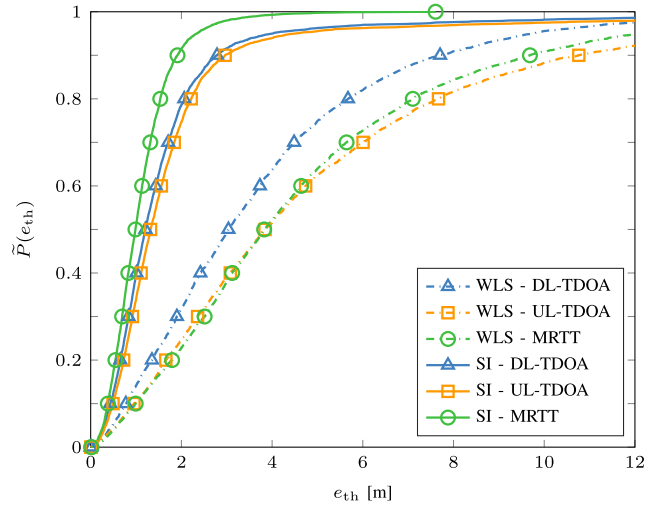

Fig. 6. ECDF for the horizontal localization error: UMi scenario and Type II simulation setting.

[13] Additional information such as NLOS detection can be employed to further improve the accuracy of SVE-based localization. Here, we aim to compare the performance of SVE-based and SI-based approaches for localization in 5G and beyond networks under the same setting, in conformity with 3GPP reports, and with the same prior information.

[14] Accuracy of single-value estimation is reported to quantify the quality of the measurements used by both localization approaches and highlight the difference in terms of wireless propagation conditions between the two scenarios considered.

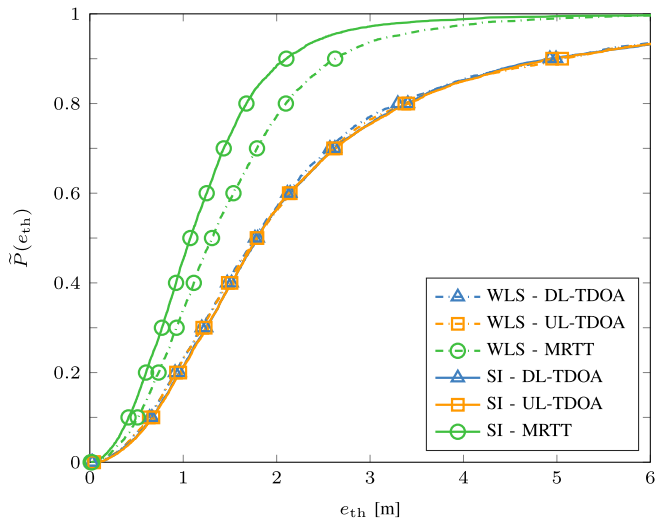

Fig. 7. ECDF for the horizontal localization error: IOO scenario and Type I simulation setting.

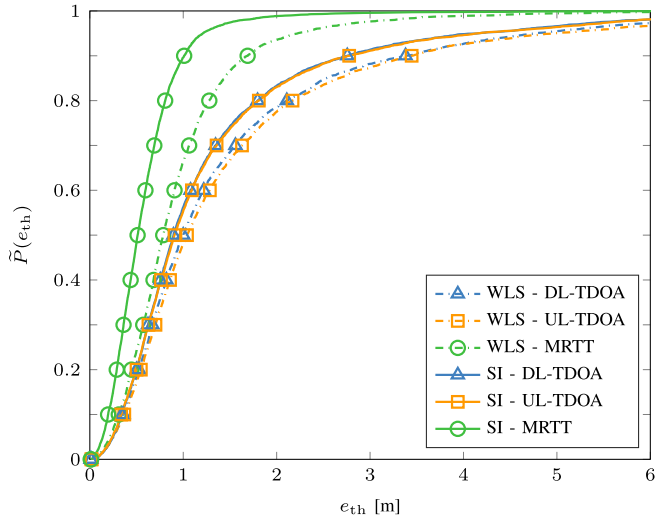

Fig. 8. ECDF for the horizontal localization error: IOO scenario and Type II simulation setting.

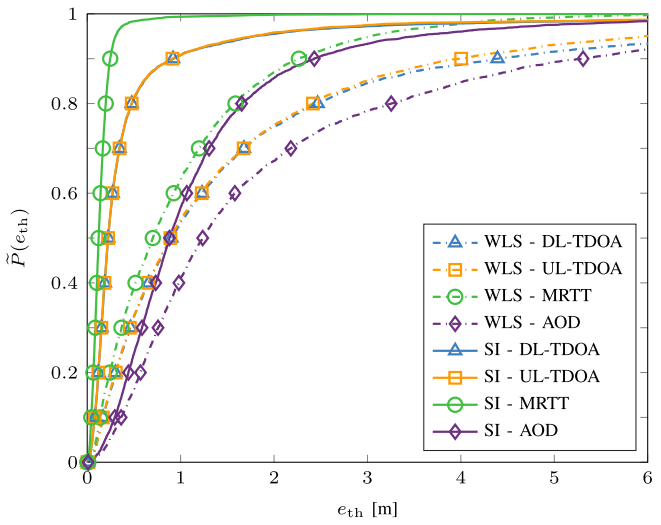

Fig. 9. ECDF for the horizontal localization error: IOO scenario and Type III simulation setting.

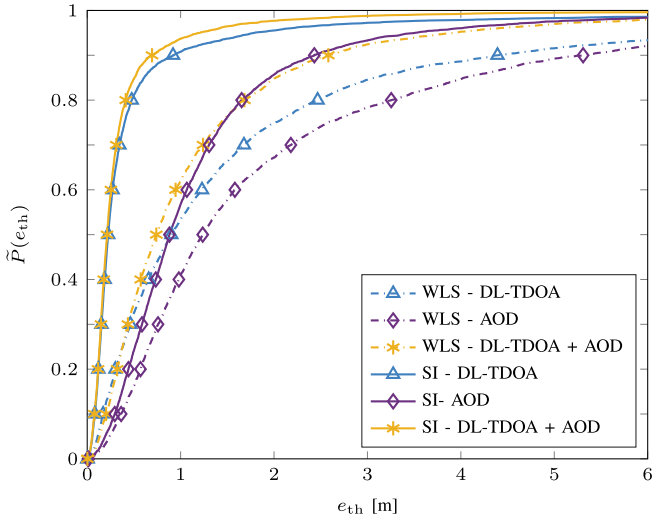

Fig. 10. ECDF for the horizontal localization error: IOO scenario and Type III simulation setting. with data fusion of DL-TDOA and AOD measurements.

B. Performance Results: UMi Scenario

Fig. 5 shows the ECDF of the horizontal localization error for the UMi scenario and Type I simulation setting. It can be observed that the SI-based approach provides significant performance improvements across all the percentiles compared to the SVE-based approach, for all 5G measurements considered. At the 80-th and 90-th percentiles, the localization accuracy improves from 4 to 8 meters compared to SVE. This can be attributed to the fact that the UMi scenario represents a harsh wireless propagation environment with a high probability of NLOS condition. In this regard, the SI-based approach via its statistical characterization is more robust compared to SVE-based approach and provides better localization accuracy. It can also be noticed that, SI-based localization exhibits the same performance for both DL-TDOA and UL-TDOA measurements despite the fact that SRS exhibits less transmitted power.

Fig. 6 shows the ECDF of the horizontal localization error for the UMi scenario and Type II simulation setting. The performance gain offered by the SI-based approach is confirmed, and even more relevant with this simulation setting. At the 90-th percentile, the SI-based approach improves the localization accuracy up to approximately 10 m for MRTT measurements compared to SVE-based. Similar gains can also be observed for DL-TDOA and UL-TDOA measurements. SI-based approach is able to fully exploit the increased RS bandwidth and provides higher localization accuracy compared to the SVE-based approach.

C. Performance Results: IOO Scenario

Fig. 7 shows the ECDF of the horizontal localization error for the IOO scenario and Type I simulation setting. It can be noticed that both SVE- and SI-based approaches provide satisfactory localization accuracy for this combination of scenario

TABLE V
90-TH PERCENTILE FOR THE HORIZONTAL LOCALIZATION ERROR FOR DIFFERENT NUMBERS OF MIXTURE IN THE GM MODEL

Scenario & Setting	**Measurement Type**	**90-th Percentile Horizontal Localization Error [m]**											
		Num. Mixture, N_{G} ($N_{\mathrm{t}} = 25000$)						**Num. Training Data, N_{t} ($N_{\mathrm{G}} = 3$)**					
		1	2	3	4	5	6	500	1000	2500	5000	10000	25000
UMi Type I	DL-TDOA	8.08	3.89	3.85	3.56	3.55	3.54	4.52	3.84	3.84	3.85	3.87	3.87
	UL-TDOA	10.19	4.01	3.81	3.63	3.60	3.63	3.93	3.85	3.82	3.83	3.81	3.81
	MRTT	9.33	3.06	2.55	2.48	2.41	2.36	2.59	2.59	2.54	2.55	2.53	2.54
UMi Type II	DL-TDOA	7.94	3.10	2.82	2.81	2.79	2.85	2.87	2.85	2.84	2.80	2.81	2.79
	UL-TDOA	13.84	3.51	2.93	2.89	2.92	2.87	3.23	3.11	2.93	3.02	2.92	2.91
	MRTT	10.81	2.75	1.94	1.85	1.79	1.64	2.39	2.29	2.31	2.06	2.10	1.96
IOO Type I	DL-TDOA	5.47	4.96	4.7	4.72	4.72	4.74	4.78	4.69	4.69	4.70	4.71	4.70
	UL-TDOA	5.44	4.94	4.68	4.70	4.72	4.69	4.78	4.76	4.76	4.70	4.70	4.67
	MRTT	2.70	2.06	2.04	2.03	2.01	2.03	2.06	2.05	2.03	2.04	2.03	2.03
IOO Type II	DL-TDOA	3.66	2.80	2.78	2.75	2.73	2.73	2.85	2.82	2.79	2.76	2.77	2.77
	UL-TDOA	3.82	2.83	2.75	2.73	2.72	2.67	2.85	2.88	2.80	2.78	2.78	2.75
	MRTT	1.86	1.02	1.02	1.00	1.00	1.03	1.04	1.02	1.02	1.02	1.02	1.02
IOO Type III	DL-TDOA	4.08	0.86	0.81	0.82	0.81	0.81	0.85	0.85	0.82	0.83	0.83	0.83
	UL-TDOA	3.68	0.87	0.84	0.84	0.82	0.82	0.86	0.85	0.84	0.86	0.84	0.84
	MRTT	1.89	0.23	0.23	0.23	0.23	0.23	0.23	0.23	0.23	0.23	0.23	0.23
	AOD	5.67	4.19	2.18	2.15	2.12	2.08	2.19	2.15	2.15	2.18	2.17	2.16

and simulation setting. The SI-based approach provides an improvement of approximately 0.5 m in terms of localization accuracy when MRTT measurements are employed. This can be attributed to the fact that in the IOO scenario, contrary to the UMi scenario, almost all the links experience LOS conditions and provide reliable measurements.

Fig. 8 shows the ECDF of the horizontal localization error for the IOO scenario and Type II simulation setting. Contrary to the Type I simulation setting, the SI-based approach outperforms the SVE-based approach. In particular, the greatest performance gain provided by SI-based approach compared to SVE-approach is experienced for MRTT measurements where SI-based localization provides approximately 0.7 m of horizontal accuracy at the 90-th percentile. On the other hand, for DL-TDOA and UL-TDOA measurement performance improvement is approximately 0.5 m. As already pointed out for the simulation results in UMi scenario and Type II simulation setting, SI-based approach takes full advantage of the increased RSs bandwidth.

Fig. 9 shows the ECDF of the horizontal localization error for the IOO scenario and Type III simulation setting. It can be observed that SI-based approach outperforms the SVE-based approach regardless of the measurement employed and it obtains sub-meter horizontal localization accuracy even at the 90-th percentile. In particular, the SI-based approach employing DL-TDOA and UL-TDOA provides approximately 0.9 m of horizontal localization accuracy 90-th percentile. For MRTT measurements, SI-based localization achieves 0.2 m horizontal accuracy at the 90-th percentile. It can also be noted that for AOD measurements SI-based approach provides approximately 1.5 m and 3 m of improvements at the 80-th and 90-th percentiles, respectively.

Fig. 10 shows the ECDF of the horizontal localization error for IOO scenario and Type III simulation setting. In this case, fusion of DL-TDOA and AOD measurements via both SVE- and SI-based approaches are considered. It can be observed that fusion of heterogeneous measurements via the SI framework provides greater performance improvements compared to the fusion based on SVEs. In particular, fusion of DL-TDOA and AOD measurements based on SI provides a performance improvement of over 4 m compared to the fusion via the SVE-based approach and an additional 0.2 m compared to the localization accuracy provided by SI exploiting DL-TDOA. It can also be noted that fusion via the SVE-based approach provides performance comparable to the ones obtained via SI based only on AOD measurements.

D. Performance Results: Generative Model Parameters

Tab. V shows the 90-th percentile for the horizontal localization error for different numbers of mixtures in the GM models and a varying number of training points for fitting the models. It can be observed that increasing N_{G} provides limited performance gains in terms of localization accuracy, especially for the IOO scenario. It can also be observed that localization based on MRTT measurements in the UMi scenario benefits the most from an increased number of Gaussian mixtures. In particular, increasing the number of mixtures in the GM model from 3 to 6 provides a performance gain of approximately 0.3 m for Type II simulation settings. This can be attributed to the fact that UMi scenario exhibits more complex propagation conditions which are better modeled by a higher number of Gaussian mixtures.

Tab. VI shows the average and standard deviation of the number of iterations required by the EM algorithm to reach convergence, assuming the parameters used to obtain the performance plots, i.e., $N_{\mathrm{G}} = 3$, $N_{\mathrm{t}} = 25000$, and $\epsilon_{\mathrm{th}} = 10^{-9}$. The values are obtained by considering the number of iterations over the 10 different training phases

TABLE VI
AVERAGE AND STANDARD DEVIATION OF THE NUMBER OF ITERATIONS REQUIRED BY EM ALGORITHM TO REACH CONVERGENCE

Scenario & Setting	Measurement Type	Average N. Iterations	Std. Deviation N. Iterations
UMi Type I	DL-TDOA	148.70	21.24
	UL-TDOA	198.90	45.41
	MRTT	303.30	63.64
UMi Type II	DL-TDOA	824.40	564.53
	UL-TDOA	190.50	42.15
	MRTT	586.20	390.58
IOO Type I	DL-TDOA	549.90	91.34
	UL-TDOA	492.50	78.60
	MRTT	263.60	10.5
IOO Type II	DL-TDOA	585.20	81.65
	UL-TDOA	721.70	134.16
	MRTT	254.80	9.56
IOO Type III	DL-TDOA	170.80	162.45
	UL-TDOA	280.40	210.75
	MRTT	228.20	113.33
	AOD	34.30	11.50

performed during the 10-fold cross-validation procedure. It can be observed that the EM algorithm is efficient and consistent in reaching convergence regardless of the measurements and scenarios considered. It can also be noted that angle-based measurements require the lowest average number of iterations for reaching convergence compared to time measurements.

VI. CONCLUSION

This paper developed SI-based localization methods that can operate with the standardized 5G architecture and extract the SI from time/angle-based measurements. The performance gain of SI-based localization methods compared to existing SVE-based methods has been quantified in different 3GPP scenarios and network settings at both sub-6 GHz and millimiter Waves. Results show that SI-based localization methods significantly outperform existing SVE-based localization methods when using time-based measurements, angle-based measurements, or fusion of the two types of measurements. The improved localization accuracy provided by the SI-based approach can support verticals and UCs for 5G and beyond networks. The SI-based approach represents an attractive solution for upcoming 3GPP standardization of 5G and beyond localization based on machine learning. The ability of SI-based localization to embrace any type of measurements makes it a candidate for providing accurate location awareness in next generation networks.

ACKNOWLEDGMENT

The authors would like to thank R. Cohen, C. A. Gomez-Vega, and G. Kwon for the careful reading of the manuscript.

REFERENCES

[1] M. Win et al., "Network localization and navigation via cooperation," *IEEE Commun. Mag.*, vol. 49, no. 5, pp. 56–62, May 2011.

[2] M. Z. Win, Y. Shen, and W. Dai, "A theoretical foundation of network localization and navigation," *Proc. IEEE*, vol. 106, no. 7, pp. 1136–1165, Jul. 2018.

[3] K. Pahlavan, X. Li, and J. P. Makela, "Indoor geolocation science and technology," *IEEE Commun. Mag.*, vol. 40, no. 2, pp. 112–118, Feb. 2002.

[4] N. Patwari, J. N. Ash, S. Kyperountas, A. O. Hero, R. L. Moses, and N. S. Correal, "Locating the nodes: Cooperative localization in wireless sensor networks," *IEEE Signal Process. Mag.*, vol. 22, no. 4, pp. 54–69, Jul. 2005.

[5] A. H. Sayed, A. Tarighat, and N. Khajehnouri, "Network-based wireless location: Challenges faced in developing techniques for accurate wireless location information," *IEEE Signal Process. Mag.*, vol. 22, no. 4, pp. 24–40, Jul. 2005.

[6] R. M. Buehrer, H. Wymeersch, and R. M. Vaghefi, "Collaborative sensor network localization: Algorithms and practical issues," *Proc. IEEE*, vol. 106, no. 6, pp. 1089–1114, Jun. 2018.

[7] A. Elzanaty, A. Guerra, F. Guidi, and M. Alouini, "Reconfigurable intelligent surfaces for localization: Position and orientation error bounds," *IEEE Trans. Signal Process.*, vol. 69, pp. 5386–5402, 2021.

[8] M. Chiani, A. Giorgetti, and E. Paolini, "Sensor radar for object tracking," *Proc. IEEE*, vol. 106, no. 6, pp. 1022–1041, Jun. 2018.

[9] J. Thomas, J. Welde, G. Loianno, K. Daniilidis, and V. Kumar, "Autonomous flight for detection, localization, and tracking of moving targets with a small quadrotor," *IEEE Robot. Autom. Lett.*, vol. 2, no. 3, pp. 1762–1769, Jul. 2017.

[10] D. Wu, D. Chatzigeorgiou, K. Youcef-Toumi, and R. Ben-Mansour, "Node localization in robotic sensor networks for pipeline inspection," *IEEE Trans. Ind. Informat.*, vol. 12, no. 2, pp. 809–819, Apr. 2016.

[11] R. Karlsson and F. Gustafsson, "The future of automotive localization algorithms: Available, reliable, and scalable localization: Anywhere and anytime," *IEEE Signal Process. Mag.*, vol. 34, no. 2, pp. 60–69, Mar. 2017.

[12] G. Zhan and W. Shi, "LOBOT: Low-cost, self-contained localization of small-sized ground robotic vehicles," *IEEE Trans. Parallel Distrib. Syst.*, vol. 24, no. 4, pp. 744–753, Apr. 2013.

[13] J. Guo, P. V. K. Borges, C. Park, and A. Gawel, "Local descriptor for robust place recognition using LiDAR intensity," *IEEE Robot. Autom. Lett.*, vol. 4, no. 2, pp. 1470–1477, Apr. 2019.

[14] D. Dardari, A. Conti, C. Buratti, and R. Verdone, "Mathematical evaluation of environmental monitoring estimation error through energy-efficient wireless sensor networks," *IEEE Trans. Mobile Comput.*, vol. 6, no. 7, pp. 790–802, Jul. 2007.

[15] F. Zabini and A. Conti, "Inhomogeneous Poisson sampling of finite-energy signals with uncertainties in $\mathbb{R}^d$," *IEEE Trans. Signal Process.*, vol. 64, no. 18, pp. 4679–4694, Sep. 2016.

[16] S. Bartoletti, A. Conti, and M. Z. Win, "Device-free counting via wideband signals," *IEEE J. Sel. Areas Commun.*, vol. 35, no. 5, pp. 1163–1174, May 2017.

[17] X. Ying, S. Roy, and R. Poovendran, "Pricing mechanisms for crowd-sensed spatial-statistics-based radio mapping," *IEEE Trans. Cognit. Commun. Netw.*, vol. 3, no. 2, pp. 242–254, Jun. 2017.

[18] R. Estrada, R. Mizouni, H. Otrok, A. Ouali, and J. Bentahar, "A crowd-sensing framework for allocation of time-constrained and location-based tasks," *IEEE Trans. Services Comput.*, vol. 13, no. 5, pp. 769–785, Sep. 2020.

[19] G. Cardone et al., "Fostering participaction in smart cities: A geo-social crowdsensing platform," *IEEE Commun. Mag.*, vol. 51, no. 6, pp. 112–119, Jun. 2013.

[20] A. Zanella, N. Bui, A. Castellani, L. Vangelista, and M. Zorzi, "Internet of Things for smart cities," *IEEE Internet Things J.*, vol. 1, no. 1, pp. 22–32, Feb. 2014.

[21] K. Lin, M. Chen, J. Deng, M. M. Hassan, and G. Fortino, "Enhanced fingerprinting and trajectory prediction for IoT localization in smart buildings," *IEEE Trans. Autom. Sci. Eng.*, vol. 13, no. 3, pp. 1294–1307, Jul. 2016.

[22] V. Moreno, M. A. Zamora, and A. F. Skarmeta, "A low-cost indoor localization system for energy sustainability in smart buildings," *IEEE Sensors J.*, vol. 16, no. 9, pp. 3246–3262, May 2016.

[23] G. Pasolini et al., "Smart city pilot projects using LoRa and IEEE802.15.4 technologies," *Sensors*, vol. 18, no. 4, p. 1118, Apr. 2018.

[24] D. Zhang, S. Zhao, L. T. Yang, M. Chen, Y. Wang, and H. Liu, "NextMe: Localization using cellular traces in Internet of Things," *IEEE Trans. Ind. Informat.*, vol. 11, no. 2, pp. 302–312, Apr. 2015.

[25] S. G. Nagarajan, P. Zhang, and I. Nevat, "Geo-spatial location estimation for Internet of Things (IoT) networks with one-way time-of-arrival via stochastic censoring," *IEEE Internet Things J.*, vol. 4, no. 1, pp. 205–214, Feb. 2017.

[26] S. D'Oro, L. Galluccio, G. Morabito, and S. Palazzo, "Exploiting object group localization in the Internet of Things: Performance analysis," *IEEE Trans. Veh. Technol.*, vol. 64, no. 8, pp. 3645–3656, Aug. 2015.

[27] J. Palacios, G. Bielsa, P. Casari, and J. Widmer, "Single- and multiple-access point indoor localization for millimeter-wave networks," *IEEE Trans. Wireless Commun.*, vol. 18, no. 3, pp. 1927–1942, Mar. 2019.

[28] C. Fiandrino, H. Assasa, P. Casari, and J. Widmer, "Scaling millimeter-wave networks to dense deployments and dynamic environments," *Proc. IEEE*, vol. 107, no. 4, pp. 732–745, Apr. 2019.

[29] *Evolved Universal Terrestrial Radio Access (E-UTRA); Study on Minimization of Drive-Tests in Next Generation Networks*, document TR 36.805 V9.0.0, Release 9, 3rd Generation Partnership Project, Jan. 2010.

[30] H. Braham, S. B. Jemaa, G. Fort, E. Moulines, and B. Sayrac, "Fixed rank Kriging for cellular coverage analysis," *IEEE Trans. Veh. Technol.*, vol. 66, no. 5, pp. 4212–4222, Aug. 2017.

[31] H. Braham, S. B. Jemaa, G. Fort, E. Moulines, and B. Sayrac, "Spatial prediction under location uncertainty in cellular networks," *IEEE Trans. Wireless Commun.*, vol. 15, no. 11, pp. 7633–7643, Nov. 2016.

[32] L. Chiaraviglio, S. Rossetti, S. Saida, S. Bartoletti, and N. Blefari-Melazzi, "'Pencil beamforming increases human exposure to electromagnetic fields': True or false?" *IEEE Access*, vol. 9, pp. 25158–25171, 2021.

[33] C. Liu et al., "Robust adaptive beam tracking for mobile millimetre wave communications," *IEEE Trans. Wireless Commun.*, vol. 20, no. 3, pp. 1918–1934, Mar. 2021.

[34] S. Fan, W. Ni, H. Tian, Z. Huang, and R. Zeng, "Carrier phase-based synchronization and high-accuracy positioning in 5G new radio cellular networks," *IEEE Trans. Commun.*, vol. 70, no. 1, pp. 564–577, Jan. 2022.

[35] *Technical Specification Group Services and System Aspects; Service Requirements for the 5G System; Stage 1 (Release 18)*, document TS 22.261 V18.5.0, Release 18, 3rd Generation Partnership Project, Dec. 2021.

[36] *Technical Specification Group Services and System Aspects; Functional Stage 2 Description of Location Services (LCS) (Release 17)*, document TS 23.271 V17.0.0, Release 17, 3rd Generation Partnership Project, Dec. 2021.

[37] *Technical Specification Group Radio Access Network; Stage 2 Functional Specification of User Equipment (UE) Positioning in UTRAN (Release 16)*, document TS 25.305 V16.0.0, Release 16, 3rd Generation Partnership Project, Jul. 2020.

[38] *Technical Specification Group Radio Access Network; Study on NR Positioning Support (Release 16)*, document TR 38.855 V16.0.0, Release 16, 3rd Generation Partnership Project, Mar. 2019.

[39] *Technical Specification Group Radio Access Network; Study on NR Positioning Enhancements (Release 17)*, document TR 38.857 V17.0.0, Release 17, 3rd Generation Partnership Project, Mar. 2021.

[40] *New SI: Study on Artificial Intelligence (AI)/Machine Learning (ML) for NR Air Interface*, Qualcomm Standard RP-213 560, Dec. 2021.

[41] J. Schloemann, H. S. Dhillon, and R. M. Buehrer, "Toward a tractable analysis of localization fundamentals in cellular networks," *IEEE Trans. Wireless Commun.*, vol. 15, no. 3, pp. 1768–1782, Mar. 2016.

[42] S. Li, M. Hedley, I. B. Collings, and D. Humphrey, "Joint trajectory and ranging offset estimation for accurate tracking in NLOS environments," *IEEE Trans. Aerosp. Electron. Syst.*, vol. 56, no. 1, pp. 3–14, Feb. 2020.

[43] *Technical Specification Group Radio Access Network; NR; Base Station (BS) Radio Transmission and Reception (Release 17)*, document TS 38.104 V17.4.0, Release 17, 3rd Generation Partnership Project, Jan. 2022.

[44] *Technical Specification Group Radio Access Network; NR; Physical Layer Measurements (Release 17)*, document TS 38.215 V17.0.0, Release 17, 3rd Generation Partnership Project, Jan. 2022.

[45] *Technical Specification Group Radio Access Network; NG Radio Access Network (NG-RAN); Stage 2 Functional Specification of User Equipment (UE) Positioning in NG-RAN (Release 16)*, document TS 38.305 V16.7.0, Release 16, 3rd Generation Partnership Project, Dec. 2021.

[46] A. Conti, S. Mazuelas, S. Bartoletti, W. C. Lindsey, and M. Z. Win, "Soft information for localization-of-things," *Proc. IEEE*, vol. 107, no. 11, pp. 2240–2264, Nov. 2019.

[47] S. Mazuelas, A. Conti, J. C. Allen, and M. Z. Win, "Soft range information for network localization," *IEEE Trans. Signal Process.*, vol. 66, no. 12, pp. 3155–3168, Jun. 2018.

[48] A. Conti et al., "Location awareness in beyond 5G networks," *IEEE Commun. Mag.*, vol. 59, no. 11, pp. 22–27, Nov. 2021.

[49] F. Morselli, S. Bartoletti, M. Z. Win, and A. Conti, "Localization in 5G ecosystem with Wi-Fi," in *Proc. IEEE 22nd Int. Workshop Signal Process. Adv. Wireless Commun. (SPAWC)*, Sep. 2021, pp. 441–445.

[50] D. C. Mur, A. Gavras, M. Ghoraishi, H. Hrasnica, and A. Kaloxylos, "AI and ML—Enablers for beyond 5G networks," 5G PPP, White Paper, May 2021, doi: 10.5281/zenodo.4299895.

[51] *Technical Specification Group Radio Access Network; Study on Channel Model for Frequencies From 0.5 to 100 GHz (Release 16)*, document TR 38.901 V16.1.0, 3rd Generation Partnership Project, Release 16, Jan. 2020.

[52] S. Dwivedi et al., "Positioning in 5G networks," *IEEE Commun. Mag.*, vol. 59, no. 11, pp. 38–44, Dec. 2021.

[53] *Evolved Universal Terrestrial Radio Access (E-UTRA); Physical Channels and Modulation*, document TS 36.211 V9.0.0, Release 9, 3rd Generation Partnership Project, Dec. 2009.

[54] *Technical Specification Group Radio Access Network; NR; Physical Channels and Modulation (Release 17)*, document TS 38.211 V17.0.0, Release 17, 3rd Generation Partnership Project, Jan. 2022.

[55] *Technical Specification Group Radio Access Network; NR; Physical Layer Procedures for Data (Release 17)*, document TS 38.214 V16.0.0, Release 17, 3rd Generation Partnership Project, Jan. 2022.

[56] *Technical Specification Group Radio Access Network; NR; Radio Resource Control (RRC) Protocol Specification (Release 16)*, document TS 38.331 V16.7.1, Release 16, 3rd Generation Partnership Project, Dec. 2021.

[57] S. Aditya, A. F. Molisch, and H. M. Behairy, "A survey on the impact of multipath on wideband time-of-arrival based localization," *Proc. IEEE*, vol. 106, no. 7, pp. 1183–1203, Jul. 2018.

[58] A. Conti, M. Guerra, D. Dardari, N. Decarli, and M. Z. Win, "Network experimentation for cooperative localization," *IEEE J. Sel. Areas Commun.*, vol. 30, no. 2, pp. 467–475, Feb. 2012.

[59] S. Bartoletti, W. Dai, A. Conti, and M. Z. Win, "A mathematical model for wideband ranging," *IEEE J. Sel. Topics Signal Process.*, vol. 9, no. 2, pp. 216–228, Mar. 2015.

[60] H. Ryden, A. A. Zaidi, S. M. Razavi, F. Gunnarsson, and I. Siomina, "Enhanced time of arrival estimation and quantization for positioning in LTE networks," in *Proc. IEEE 27th Annu. Int. Symp. Pers., Indoor, Mobile Radio Commun. (PIMRC)*, Sep. 2016, pp. 1–6.

[61] C. Mensing and S. Plass, "Positioning algorithms for cellular networks using TDOA," in *Proc. IEEE Int. Conf. Acoust. Speed Signal Process.*, Dec. 2006, p. 4.

[62] H. Rydén et al., "Baseline performance of LTE positioning in 3GPP 3D MIMO indoor user scenarios," in *Proc. Int. Conf. Localization GNSS (ICL-GNSS)*, Jun. 2015, pp. 1–6.

[63] R. Zekavat and R. M. Buehrer, *Handbook of Position Location: Theory, Practice and Advances*, vol. 27. Hoboken, NJ, USA: Wiley, 2011.

[64] J. Kennedy and R. C. Eberhart, "Particle swarm optimization," in *Proc. IEEE Int. Conf. Neural Netw.*, vol. 4, Nov./Dec. 1995, pp. 1942–1948.

[65] K. Cheung, H. So, W.-K. Ma, and Y. Chan, "A constrained least squares approach to mobile positioning: Algorithms and optimality," *EURASIP J. Adv. Signal Process.*, vol. 2006, no. 1, pp. 1–23, Dec. 2006.

[66] C. Yang, Y. Huang, and X. Zhu, "Hybrid TDOA/AOA method for indoor positioning systems," in *The Institution of Engineering and Technology Seminar on Location Technologies*, Institute of Engineering and Technology, 2007, pp. 1–5.

[67] *Technical Specification Group Radio Access Network; LTE Positioning Protocol (LPP) (Release 16)*, document TS 37.355 V16.7.0, Release 16, 3rd Generation Partnership Project, Dec. 2021.

[68] *Technical Specification Group Radio Access Network; NG-RAN; NR Positioning Protocol A (NRPPa) (Release 16)*, document TS 38.455 V16.6.0, Release 16, 3rd Generation Partnership Project, Dec. 2021.

[69] C. M. Bishop, *Pattern Recognition and Machine Learning*. New York, NY, USA: Springer-Verlag, 2006.

[70] J. S. Klemelä, *Smoothing of Multivariate Data: Density Estimation and Visualization*. Hoboken, NJ, USA: Wiley, 2009, vol. 737.

[71] D. J. MacKay, *Information Theory, Inference, and Learning Algorithms*. New York, NY, USA: Cambridge Univ. Press, 2003.

[72] S. Arlot and A. Celisse, "A survey of cross-validation procedures for model selection," *Statist. Surveys*, vol. 4, pp. 40–79, May 2010.

[73] *Technical Specification Group Radio Access Network; Study on New Radio Access Technology Physical Layer Aspects (Release 16)*, document TR 38.802 V14.2.0, Release 14, 3rd Generation Partnership Project, Mar. 2017.

[74] S. Jaeckel, L. Raschkowski, K. Borner, and L. Thiele, "QuaDRiGa: A 3-D multi-cell channel model with time evolution for enabling virtual field trials," *IEEE Trans. Antennas Propag.*, vol. 62, no. 6, pp. 3242–3256, Jun. 2014.

[75] *System Level Performance Evaluation for RAT-Dependent Positioning Techniques*, Ericsson Std. R1-1 903 142, Feb. 2019.

[76] *3rd Generation Partnership Project; Technical Specification Group Radio Access Network; Evolved Universal Terrestrial Radio Access (E-UTRA); Requirements for Support of Radio Resource Management (Release 16)*, document TS 36.133 V16.7.0, Release 16, 3rd Generation Partnership Project, Oct. 2020.

Flavio Morselli received the Laurea degree in electronics and telecommunications engineering and the Ph.D. degree in engineering science–information engineering from the University of Ferrara, Italy, in 2017 and 2022, respectively.

From 2017 to 2022, he was a Research Assistant with the Wireless Communication and Localization Networks Laboratory at University of Ferrara. From 2019 to 2022, he was a Research Assistant with the Consorzio Nazionale Interuniversitario per le Telecomunicazioni (CNIT). He is currently a Software Engineer with JMA Wireless, his work mainly involves research and development of full-software solutions for positioning in the 5G RAN. His research interests include network localization and navigation, multi-target tracking, and stochastic sampling.

Dr. Morselli served as a reviewer for several IEEE journals and conferences.

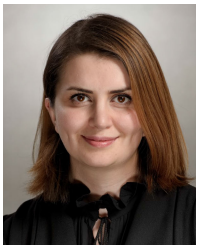

Sara Modarres Razavi received the M.Sc. degree in hardware for wireless communication from the Chalmers University of Technology, Sweden, in 2006, and the Ph.D. degree in infra-informatics from Linköping University in 2014.

In 2014, she joined Ericsson Research. She has been the Cloud RAN Innovation Program Manager at Ericsson, Stockholm, Sweden, since 2022. Prior to this role, she was a Master Researcher and the 3GPP Standardization Project Manager of 5G and 5G advanced standardization.

Her published contributions include more than 30 peer reviewed articles and more than 100 filed patents mainly on the area of positioning in wireless networks. Her main research interests include 4G/5G/6G cellular networks, positioning, radio resource optimization, tracking area management, and massive and critical IoT communication. In the area of localization, she has taken many leading roles.

Moe Z. Win (Fellow, IEEE) is a Professor at the Massachusetts Institute of Technology (MIT) and the founding director of the Wireless Information and Network Sciences Laboratory. Prior to joining MIT, he was with AT&T Research Laboratories and with NASA Jet Propulsion Laboratory.

His research encompasses fundamental theories, algorithm design, and network experimentation for a broad range of real-world problems. His current research topics include ultra-wideband systems, network localization and navigation, network interference exploitation, and quantum information science. He has served the IEEE Communications Society as an elected Member-at-Large on the Board of Governors, as elected Chair of the Radio Communications Committee, and as an IEEE Distinguished Lecturer. Over the last two decades, he held various editorial positions for IEEE journals and organized numerous international conferences. Recently, he has served on the SIAM Diversity Advisory Committee.

Dr. Win is an elected Fellow of the AAAS, the EURASIP, the IEEE, and the IET. He was honored with two IEEE Technical Field Awards: the IEEE Kiyo Tomiyasu Award (2011) and the IEEE Eric E. Sumner Award (2006, jointly with R. A. Scholtz). His publications, co-authored with students and colleagues, have received several awards. Other recognitions include the MIT Everett Moore Baker Award (2022), the IEEE Vehicular Technology Society James Evans Avant Garde Award (2022), the IEEE Communications Society Edwin H. Armstrong Achievement Award (2016), the Cristoforo Colombo International Prize for Communications (2013), the Copernicus Fellowship (2011) and the *Laurea Honoris Causa* (2008) from the Università degli Studi di Ferrara, and the U.S. Presidential Early Career Award for Scientists and Engineers (2004). He is an ISI Highly Cited Researcher.

Andrea Conti (Fellow, IEEE) is a Professor and the founding Director of the Wireless Communication and Localization Networks Laboratory, University of Ferrara, Italy. Prior to joining at the University of Ferrara, he was with CNIT and IEIIT-CNR.

In Summer 2001, he was with the Wireless Systems Research Department, AT&T Research Laboratories. Since 2003, he has been a Frequent Visitor with the Wireless Information and Network Sciences Laboratory, Massachusetts Institute of Technology, Cambridge, MA, USA, where he currently holds the Research Affiliate appointment. His research interests involve theory and experimentation of wireless communication and localization systems. His current research interests include network localization and navigation, distributed sensing, adaptive diversity communications, and quantum information science.

Dr. Conti has served as an editor for IEEE journals and chaired international conferences. He was an elected Chair of the IEEE Communications Society's Radio Communications Technical Committee. He is the Co-Founder of the IEEE Quantum Communications and Information Technology Emerging Technical Subcommittee. He was a recipient of the HTE Puskás Tivadar Medal, the IEEE Communications Society's Fred W. Ellersick Prize, and the IEEE Communications Society's Stephen O. Rice Prize in the field of Communications Theory. He is elected as a fellow of the IET and a member of Sigma Xi. He has been selected as an IEEE Distinguished Lecturer.

Open Access funding provided by 'Università degli Studi di Ferrara' within the CRUI CARE Agreement